ABSTRACT

Title of Dissertation: A NEW ROLE FOR THE CYT-18 N-TERMINUS AND THREE-DIMENSIONAL DNA CRYSTALS AS VEHICLES FOR BIOCATALYSIS

Chun Geng, Doctor of Philosophy, 2014

Dissertation Directed By: Paul J. Paukstelis
Department of Chemistry and Biochemistry
Center for Biomolecular Structure and Organization

The bifunctional *Neurospora crassa* mitochondrial tyrosyl-tRNA synthetase (*N. crassa* mt TyrRS; CYT-18 protein) promotes the splicing of multiple group I introns by stabilizing the catalytically active intron structures. CYT-18, and mt TyrRS's from related fungal species, have evolved to promote group I intron splicing partly by accumulation of three N-terminal domain insertions that create a structure-stabilizing scaffold for critical tertiary interactions between the two major group I intron domains. The primarily α-helical N-terminal insertion, H0, contributes to protein stability and is necessary for splicing the *N. crassa* ND1 intron, but is dispensable for splicing the *N. crassa* mt LSU intron. Herein, I show CYT-18 with a complete H0 deletion retains residual ND1 intron splicing activity and addition of the missing N-terminus *in trans* restores a significant portion of its splicing activity. This peptide complementation assay revealed important characteristics of the CYT-18/group I intron interaction including the stoichiometry of H0 in intron splicing and

the importance of specific H0 residues. Evaluation of truncated H0 peptides in this assay also suggests a previously unknown structural role of the first five N-terminal residues of CYT-18. These residues interact directly with another splicing insertion, making H0 a central structural element responsible for connecting all three N-terminal splicing insertions.

Transitioning to a separate study, I have demonstrated that enzymes retain catalytic activity when captured in the solvent channels of three-dimensional (3D) DNA crystals. Using RNase A as a model enzyme system this work shows that crystals infused with enzyme can cleave a fluorescent dinucleotide substrate with similar kinetic restrictions as other immobilized enzyme systems, mainly limited by diffusion of substrate. This new vehicle for immobilized enzymes, created entirely from biomolecules, provides a platform for developing modular solid-state catalysts that could be both biocompatible and biodegradable.

A NEW ROLE FOR THE CYT-18 N-TERMINUS AND THREE-DIMENSIONAL DNA CRYSTALS AS VEHICLES FOR BIOCATALYSIS

By

Chun Geng

Dissertation submitted to the Faculty of the Graduate School of the
University of Maryland, College Park, in partial fulfillment
of the requirements for the degree of
Doctor of Philosophy
2014

Advisory Committee:
Professor Paul Paukstelis, Chair
Professor Kwaku Dayie
Professor David Fushman
Professor Nicole LaRonde
Professor Wenxia Song, Dean's Representative

Dedication

To my father, Kexiang Geng

and mother, Kun Wan

who encourage me to go on every adventure,

especially this one

Acknowledgements

I would like to give my sincere gratitude to the following people who never ceased in helping me until this dissertation is structured:

Prof. Paul Paukstelis for the opportunities and generous support he has been constantly giving me. Without him, this dissertation would not be possible;

Profs. Kwaku Dayie, David Fushman, and Nicole LaRonde for serving as my dissertation committee and continually giving me encouragement and suggestions;

Prof. Wenxia Song for dedicating her time as the Dean's Representative;

All past and present members of the Paukstelis group, especially Ryan Griffis, Stephanie Muser, Maithili Saoji and Diana Zhang for the moral and technical support;

Drs. Mark Nakasone and Daoning Zhang for the helpful ideas;

Lei Li and Prof. Zhengguo Xiao for their insight on the dot blotting work;

Prof. Dorothy Beckett for the useful advices and isothermal calorimetry trial;

Prof. George Lorimer for the fluorometer usage;

Prof. Jason Kahn for the atomic force microscope usage;

Prof. Douglas Julin for the useful advice and support;

Drs. Vitali Tugarinov and Chenyun Guo for the pre-candidacy advising;

Paulette Frazier and Judith Mahaffy for their administrative support;

Dr. Amy Beaven for providing the confocal microscope training;

Dr. Yue Li for the mass spectrometry support;

Zifan for providing the love I have needed. Without her, I would not be where I am today.

Table of Contents

List of Tables

List of Figures

PART I: A NEW ROLE FOR THE CYT-18 N-TERMINUS

Chapter 1: Introduction

1.1 Group I introns

Introns are the non-coding regions of a gene that must be properly removed by RNA splicing from exons.[1, 2] According to the specific splicing mechanisms, several classes of introns have been identified, including spliceosomal introns, tRNA introns, as well as group I and group II introns.[1] Through the past thirty years of intense study, group I introns have become the best understood, with respect to their tertiary RNA structure and splicing mechanism.[3-8]

Group I introns are widely distributed in bacteria, viruses, chloroplasts, and mitochondrial genomes but are not found in humans.[9, 10] Being the first RNAs that are demonstrated to be catalytically active[11, 12], group I introns utilize a splicing mechanism[10] that begins with the attack of the 3' hydroxyl group of a guanosine at the 5' splice site and is followed by the attack of the 3' hydroxyl of the 5' exon at the 3' exon. The splicing is completed with the ligation of two exons and the excision of the intron **(Figure 1.1)**. Group I introns have limited sequence homology but share conserved secondary/tertiary structures[5-7] and the same splicing mechanism[10]. The conserved group I intron secondary structure consists of base-paired regions (P), junction regions (J) between the base-paired helices, and loop regions (L) that join the base-paired stem regions **(Figure 1.2A)**.[5] Nine conserved base-paired regions (P1-P9) fold into two extended helical domains, designated as P4-P6 and P3-P9, which are

juxtaposed to form the active site cleft for splicing when they are aligned in the right orientation **(Figure 1.2B)**.[3-5, 13, 14] The J3/4 and J6/7 nucleotide triples in P6's minor groove and P4's major groove are important in determining the relative orientation of the P4-P6 and P3-P9 domains.[3-5, 15] In addition, the tetraloop-tetraloop receptor interactions between L9 and P5,[13] interactions between L2 and P8,[16] and interactions between P5abc and other peripheral elements and the catalytic core[17] all provide further stability. Though some group I introns can self-splice *in vitro*, requiring only guanosine and magnesium, many group I introns including *N. crassa* ND1 and mitochondrial LSU introns are not capable of efficient splicing without the aid of cofactors *in vivo*.[15] Many protein splicing cofactors have been studied.[18-23] The first discovered and most extensively studied is CYT-18, a protein splicing cofactor promoting the splicing of group I introns primarily by binding and stabilizing a catalytically active RNA conformation.[24-29]

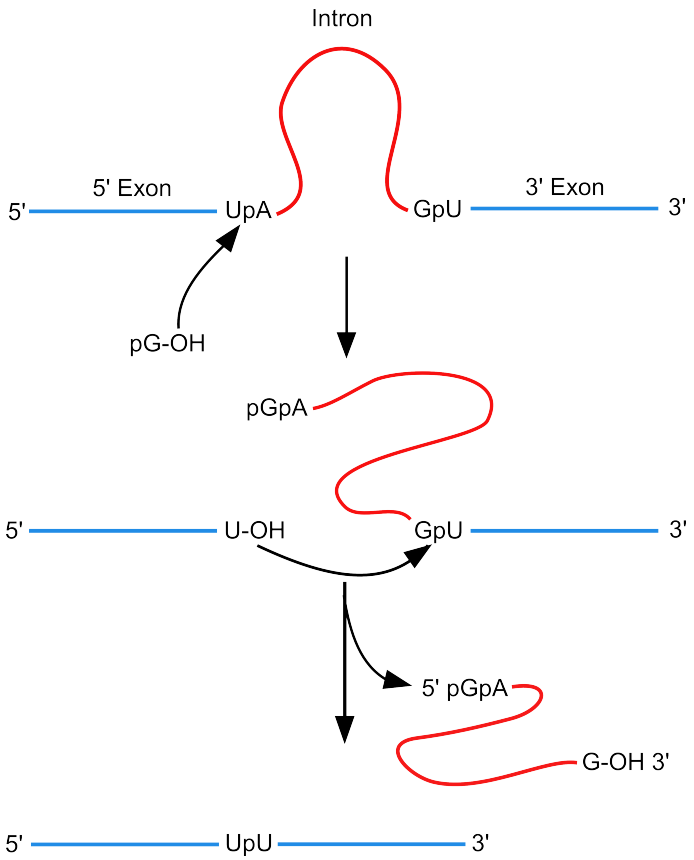

Figure 1.1 - Splicing mechanism for group I intron.
Group I introns utilizes a splicing mechanism through two trans-esterification reactions. It begins with the attack of the 3' hydroxyl group of a guanosine at the 5' splice site and is followed by the attack of the 3' hydroxyl of the 5' exon at the 3' exon. The splicing is completed with the ligation of two exons and the excision of the intron.[10]

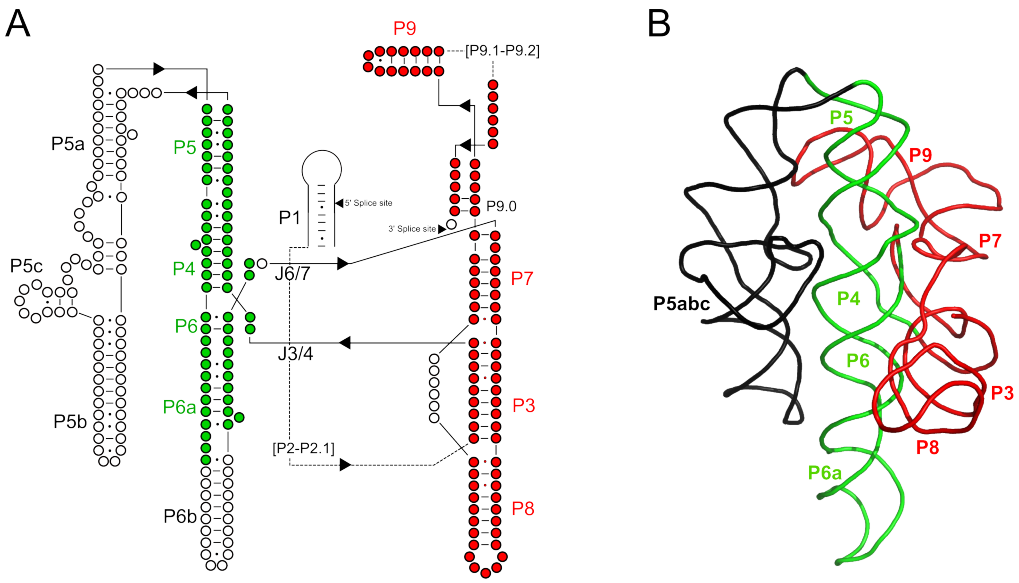

Figure 1.2 - Secondary structure (A) and tertiary structure (B) of group I intron *Tetrahymena* ribozyme.
(A) Conserved helical base-pairing regions are designated P1 through P9.2, and joining regions are designated with a "J". P4-P6 domain is colored in green, P3-P9 domain is colored in red, and the peripheral extensions are colored in black. **(B)** Tertiary crystal structure of the *Tetrahymena thermophila* rRNA LSU group I intron, showing P4-P6 and P3-P9 domains juxtaposed to form the active site for splicing. The domains are colored as in **(A)**.[14] PDB ID: 1GRZ.

1.2 CYT-18 and the N-terminal extension H0

The *N. crassa* mitochondrial tyrosyl-tRNA synthetase (mt TyrRS; CYT-18 protein) and the mt TyrRS's from other Pezizomycotina fungi are multifunctional proteins responsible for aminoacylating mt $tRNA^{Tyr}$ and promoting mt group I intron splicing.[24, 30] CYT-18 is a homodimer, which binds one molecule of group I intron RNA.[31] Previous studies showed that CYT-18 recognizes conserved structural features of the group I intron catalytic core and promotes splicing by stabilizing the catalytically active RNA structure.[25-27] Chemical structure modification analysis showed that CYT-18 does not recognize introns in a sequence-specific manner but instead recognizes the three-dimensional structure of the phosphodiester backbone.[27, 28] Though group I intron primary sequences can vary greatly, their conserved three-dimensional structures allow CYT-18 to recognize and promote splicing of diverse group I introns.[26, 32-34] Biochemical and genetic experiments led to a model describing how CYT-18 functions in splicing; first interacting with the intron P4−P6 domain and then contacting the P3−P9 domain, which stabilizes the two extended RNA domains in the correct orientation relative to non-native structures to generate a catalytically active intron conformation.[25-27, 32, 35]

Similar to CYT-18, the bacterial TyrRS's are homodimers, which bind and aminoacylate one molecule of $tRNA^{Tyr}$ ("half-of-sites reactivity").[36] The extensively studied structures of bacterial TyrRS's are comprised of an N-terminal nucleotide-binding fold, an intermediate α-helical domain, and a C-terminal tRNA-binding domain, which fold into a structurally conserved TyrRS core.[37] Sequence analysis showed the mt TyrRS's of Pezizomycotina species are distinguished by six

positionally conserved distinct insertions, including an N-terminal extension (H0), two small insertions in the catalytic domain (Ins1 and Ins2), and three insertions in the C-terminal domain (Ins3, Ins4, and Ins5), which are absent in the bacterial TyrRS's or yeast mt TyrRS.[30, 38] Superimposition of the crystal structures of a C-terminally truncated CYT-18 and *Bacillus stearothermophilus* TyrRS demonstrate close structural similarity in their TyrRS cores including the nucleotide-binding fold and α-helical intermediate domain except for the three CYT-18-specific insertions **(Figure 1.3)**.[39] Despite the significant structural homology between bacterial and mt TyrRS's, the activity to promote group I intron splicing has only been demonstrated for mt TyrRS's of fungi (*Aspergillus nidulans*, *Histoplasma capsulatum* and *Podospora anserina*) belonging to the subphylum Pezizomycotina.[30]

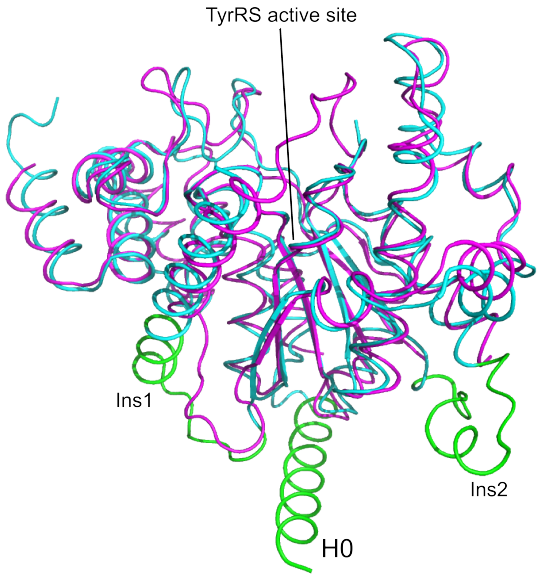

Figure 1.3 - Ribbon diagram showing structural overlap of the nucleotide binding fold and α-helical domains of monomeric CYT-18/ΔC424−669 and *B. stearothermophilus* TyrRS.
The *B. stearothermophilus* TyrRS monomer structure (purple, PDB ID: 3TS1[37]) was superimposed on that of CYT-18 (cyan and green, PDB ID: 1Y42[39]). CYT-18-specific insertions are in green.

Of the three N-terminal insertions, the N-terminal extension H0 has the highest sequence conservation among the Pezizomycotina mt TyrRS's and is the most thoroughly studied biochemically.[30, 40] H0 (residues 33-61) is primarily an amphipathic α-helix (residues 39-60) that represents the first regular secondary structural element of CYT-18 following cleavage of the mt targeting peptide (residues 1-32). Previous biochemical studies demonstrated that H0 is important for intron splicing but dispensable for the tyrosyl tRNA synthetase activities.[40] In the previous work, all the CYT-18 N-terminal truncations tested partially retained the N-terminal-most residues and began only after Phe37. Deletion of as few as four residues (Δ38−41) abolished the splicing activity.[38] However, an even more extensive deletion that included the entire H0 α-helix (Δ38−59) retained the splicing activity for the mt LSU intron but was unable to splice the *N. crassa* ND1 intron.[40] Conversely, the C-terminal domain of CYT-18 was required for splicing the *N. crassa* mt LSU intron but was dispensable for splicing the ND1 intron. This observed differential dependence on these structural elements suggested that CYT-18 utilizes different regions to compensate for different RNA structural defects in non-self-splicing group I introns.[40]

Structures mainly resulting from X-ray crystallography have provided significant information for elucidating the structural and functional role of H0 in group I intron splicing. The crystal structure of a C-terminally truncated CYT-18 (CYT-18/Δ424−669) showed that H0 is connected to the highly conserved TyrRS core through Gly62 and H0 is stabilized against the protein core by primarily localized hydrophobic interactions through H0 residues Trp52, Arg55, and Ile59.[39]

This structural evidence is consistent with the genetic experiments that identified these residues as among the most highly conserved in splicing-competent proteins from H0 mutant libraries.[40] However, due to the weak electron density and ambiguity of the seven N-terminal-most residues of H0 (including the initiating Met that is not present in the mature protein in mt) and the flexible C-terminal residues from a symmetry-related monomer, these N-terminal residues were not built in the crystal structure.[39]

Another structure of a splicing-active C-terminally truncated CYT-18 protein (CYT-18/Δ424−669) co-crystallized with a group I intron RNA (the bacteriophage Twort *orf*142-I2 ribozyme) revealed key structural features of RNA-protein interactions **(Figure 1.4)**. It showed that H0, Ins1, and Ins2 from one subunit (Subunit B) of the homodimer, directly interact with the group I intron catalytic core and stabilize and/or promote key tertiary RNA-protein interactions.[15] The structural information revealed by this work indicate that H0 and Ins1 of one subunit interact with each other through side chain contacts to form a distinct structural scaffold for group I intron binding at its junction of the two RNA domains, with Ins2 of the same CYT-18 subunit interacting in the minor groove of the intron's P9 helix. Based on the co-crystal structure, H0 from one subunit of the CYT-18 dimer assists in establishing the correct orientation of the P4-P6 and P3-P9 of the group I intron through interactions with the two major junctions, J3/4 and J6/7, as well as P7. H0 from the other subunit of the CYT-18 dimer is in close proximity to the P5 domain of the group I intron, but its role in group I intron splicing is not clear. Although the co-crystal structure was determined at low-resolution (4.5 Å), the structure showed

contiguous backbone electron density for the previously unobserved N-terminal H0 residues.

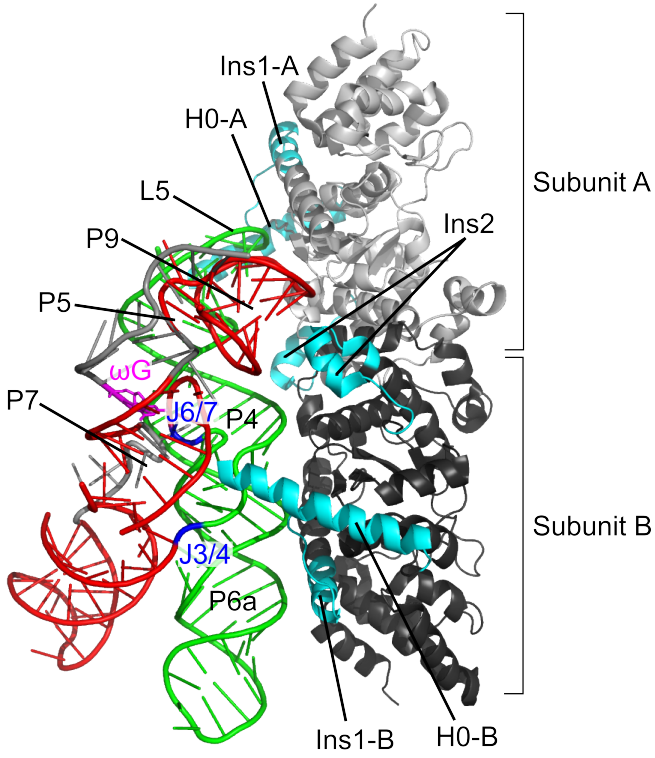

Figure 1.4 - Cartoon diagram showing CYT-18 interacting and stabilizing the Twort *orf*142-I2 intron structure.
CYT-18 (right, two subunits are colored grey and black) interacts with the intron's P4−P6 domain (middle, green), followed by contacts with the P3−P9 domain (left, red) that stabilize the two extended RNA domains in the correct orientation relative to non-native structures to generate a catalytically active intron conformation. The group intron domains are colored as in **Figure 1.2**. J3/4 and J6/7 are colored in blue; ωG is colored in pink, respectively. PDB ID: 2RKJ.[12]

This prior work allowed me to expand on the structural and functional roles of H0 in group I intron splicing and pioneer an *in vitro* peptide complementation splicing assay. Studies on the first complete H0 deletion on CYT-18 (CYT-18/Δ33−61) showed that it retains residual splicing activity. My work herein shows the splicing activity of CYT-18/Δ33−61 is significantly restored by the addition of the N-terminal H0 peptide *in trans*. Titration experiments coupled with burst kinetic analysis indicate that H0 bound to one subunit of the CYT-18 dimer is sufficient to promote splicing of the group I intron. The failure of short N-terminally truncated H0 peptides to restore splicing in this assay and the inability of a CYT-18 mutant lacking just the first five H0 residues to promote splicing indicate a previously unrecognized role for the N-terminal-most residues of CYT-18. A reanalysis of the CYT-18/Δ424−669 crystal structure indicates that these N-terminal residues interact directly with Ins2, which provides a new role for H0 as a structural link connecting all three N-terminal splicing insertions.

Chapter 2: Experimental Procedures

2.1 Protein expression and purification

The wild-type CYT-18 protein was expressed in *Escherichia coli* (*E. coli*) HMS174(DE3) cell from plasmid pEX560[40] and purified by polyethyleneimine (PEI) precipitation[31] and ion-exchange chromatography with 15-Q and 15-S columns (GE Healthcare Bio-Sciences, Pittsburgh, PA), with the 15-S column eluted by a linear gradient of 0.025-1 M KCl in 25 mM Tris-HCl (pH 7.5), 10% glycerol. All steps were performed at 4 °C. The CYT-18/Δ33−61 and CYT-18/Δ33−37 open reading frames, both with an N-terminal hexahistidine tag followed by a tobacco etch virus (TEV) protease recognition sequence, were cloned into expression vector pET-11d (Novagen) and confirmed by sequencing. Both proteins were expressed by autoinduction[41] in *E. coli* HMS174(DE3) cell and purified by a Ni^{2+} column, TEV cleavage, a second Ni^{2+} column, and a final Superdex S-200 gel filtration column[30]. All proteins were dialyzed against 25 mM Tris-HCl (pH 7.5), 500 mM KCl, and 50% (v/v) glycerol, flash frozen, and stored at − 80 °C. The active concentrations of protein were determined by tyrosyl-adenylation assays as described below.

2.2 Denaturation and renaturation

Protein denaturation was done by mixing 200 μL of 100 μM CYT-18 dimer with1.8 mL of denaturation buffer containing 25 mM Tris-HCl (pH 7.5), 500 mM KCl, 2 mM DTT, and 8 M urea, followed by a 10-minute (min) incubation. Protein renaturation was done by buffer exchange using an Amicon Ultra 10K MWCO centrifugal filter concentrator. The urea was gradually removed by four cycles of

centrifugation. A total of 4.5 mL of renaturation buffer containing 25 mM Tris-HCl (pH 7.5) and 500 mM KCl was added to the concentrator following concentration to 250 μL (in the renaturation with H0-WT experiment, 6-fold molar excess of H0-WT with respect to the initial concentration of protein is also added). The final protein concentrations were determined by UV absorbance at 280 nm (A_{280}) and adjusted to 500 nM for tyrosyl-adenylation assays (ε_{280} for CYT-18, CYT-18/Δ33−61 and CYT-18/Δ33−37 are respectively 96680 M^{-1} cm^{-1}, 89710 M^{-1} cm^{-1}, and 96680 M^{-1} cm^{-1}). All steps were performed at 25 °C.

2.3 Peptide synthesis, expression, and purification

Except where noted, peptides utilized in the complementation assays were chemically synthesized, HPLC-purified, and lyophilized (United Biosystems, Herndon, VA and NEO Biolab, Cambridge, MA). These peptides were directly dissolved in 10 mM Tris-HCl (pH 7.5), 10 mM KCl, and 50% (v/v) glycerol and stored at − 80 °C. Several assays were performed with recombinant H0-WT peptide. The H0-WT peptide was cloned into vector pMAL-C2T, expressed via autoinduction in *E. coli* HMS174(DE3) cell as a maltose-binding protein (MBP) fusion that was cleavable by TEV protease. The fusion protein was purified by amylose affinity chromatography and cleaved by TEV protease overnight at 4°C. The H0-WT peptide was further purified by size-exclusion chromatography **(Figure 2.1)**. Both synthetic and recombinant peptides were verified by mass spectrometry. Concentrations were determined by A_{280} (ε_{280} for H0-WT, H0-37, H0-42, and H0-46 are respectively 6970 M^{-1} cm^{-1}, 6970 M^{-1} cm^{-1}, 5690 M^{-1} cm^{-1}, and 5690 M^{-1} cm^{-1}).

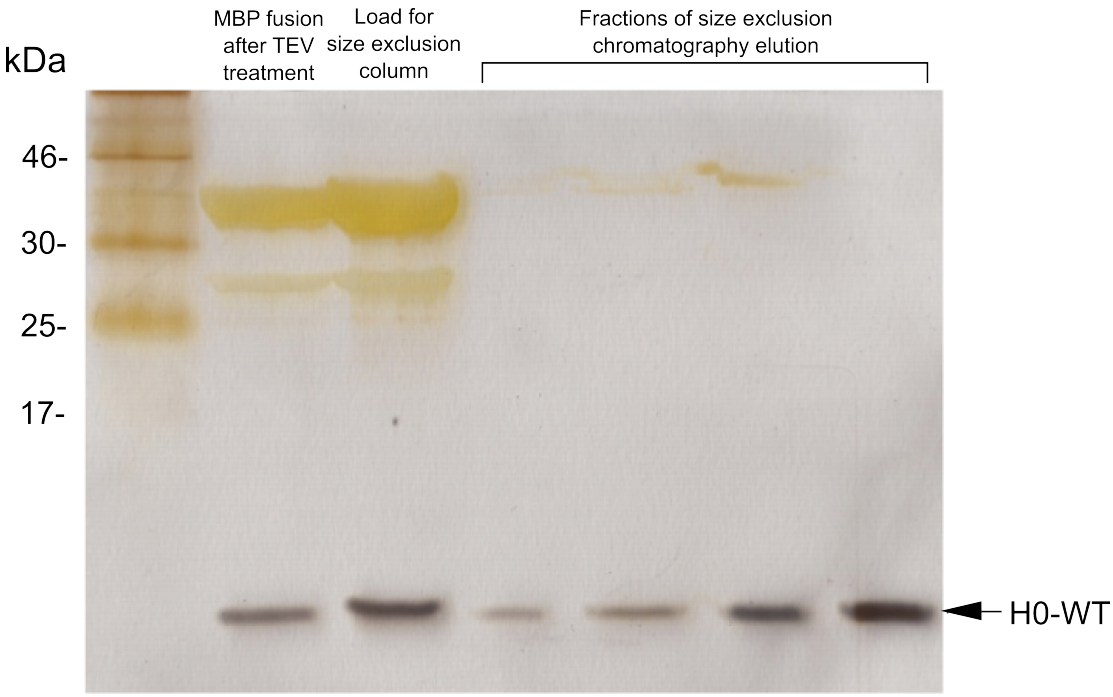

Figure 2.1 - Silver-stained SDS-PAGE gel for H0-WT purification.
This gel shows the MBP fusion sample after TEV protease treatment and fractions of the size exclusion chromatography. The H0-WT peptide, with an estimated molecular weight of 3.6 kDa, is quantified to be > 95% pure according to the fraction from which the final H0-WT was collected (the last lane).

2.4 Tyrosyl-adenylation assay

Tyrosyl-adenylation assays were done in 25 μL of reaction containing 500 nM protein, 5 mM ATP, 100 mM KCl, 10 mM $MgCl_2$, 144 mM Tris-HCl (pH 7.5), 0.1 unit of pyrophosphatase, and 5 μCi of L-[3,5-^{3}H]-tyrosine (42.6 Ci mmol^{-1}; Perkin-Elmer). The reaction was initiated by addition of protein and incubated for 10 min at 30 °C. The samples were then filtered through nitrocellulose membrane (0.2 μm pore size) to retain protein-bound tyrosyl-adenylate. Membranes were counted with a Beckman Coulter model LS6500 scintillation counter with ScintiVerse I scintillation cocktail (Fisher Scientific).

2.5 Group I intron splicing

^{32}P-labeled RNA substrates were synthesized by *in vitro* transcription from linearized plasmids, using MEGAscript kit (Ambion) with 3.3 mM [α-^{32}P] UTP (0.445 Ci mmol^{-1}; PerkinElmer).[30] Splicing assays were done by adding CYT-18 protein to ^{32}P-labeled RNA substrate to a final reaction volume of 25 μL containing 5 mM $MgCl_2$, 25 mM Tris-HCl (pH 7.5), 1 mM DTT, 10% glycerol, 1 mM GTP-Mg^{2+}, and indicated amount of KCl at specified temperatures. Splicing products were analyzed in either a 4% or 6% denaturing polyacrylamide gel that was dried and quantified with a Storm PhosphorImager (GE Bioscience). For peptide complementation experiments, indicated amounts of H0-WT or truncated H0 peptides were incubated with the CYT-18/Δ33−61 protein at 25 °C for 1 hour (h) before being added to the splicing reaction. Burst kinetic analysis was done by incubating

indicated amounts of CYT-18 protein with a 2-fold molar excess of ^{32}P-labeled RNA substrate in the described splicing conditions lacking GTP-Mg^{2+}. These reactions were initiated by addition of 1 mM GTP-Mg^{2+}.

2.6 RNA equilibrium binding assay

25 μL reactions were set up as described in the group I intron splicing and peptide complementation assays with GTP omitted. After incubating for 1 h at 25°C, within a 96-well vacuum manifold (Schleicher & Schuell), 5 μL of each reaction was spotted directly on to layered nitrocellulose (0.2 μm pore size; Invitrogen) and nylon (Hybond-N; Amersham) membranes that were presoaked in the splicing buffer with 50 mM KCl. The membranes were washed three times with 250 μL of the same splicing buffer, dried and then quantified with a Storm PhosphorImager. The disintegrations per minute (DPM) values on nitrocellulose membrane were divided by the sum of DPM values from both the nitrocellulose and nylon membranes. The calculated percentages of the protein-bound ^{32}P RNA out of the total ^{32}P RNA input were then normalized with respect to the wild-type CYT-18.

Chapter 3: Functional Assays and Stability of CYT-18/Δ33−61

3.1 The first mutant of CYT-18 with a complete H0 deletion

As described in Chapter 1, the previous CYT-18 N-terminal truncations constructed to study H0 (residues 33-61) all began after Phe37.[38, 40] In order to further examine the role of the CYT-18-specific H0 insertion, and develop a peptide complementation assay, I constructed the first mutant of CYT-18 with a complete H0 deletion **(Figure 3.1)**. This mutant (CYT-18/Δ33−61) was generated through addition of an N-terminal hexahistidine tag followed by a protease cleavage site (Chapter 2). Immobilized metal affinity purification steps before and after removal of the 6XHis tag with TEV protease yielded > 95% pure protein (judged by the Coomassie stained SDS-PAGE gel, **Figure 3.2**) with native Gly62 as the N-terminal-most residue. The purification method as described in Chapter 2 via a Ni^{2+} column, TEV cleavage, and a second Ni^{2+} column enabled me to maintain high monovalent salt and glycerol concentrations throughout the purification, which was necessary to help maintain the protein solubility.

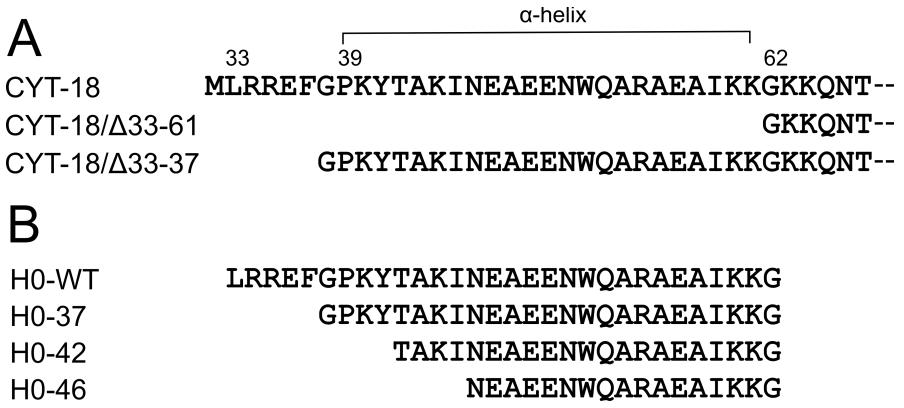

Figure 3.1 - CYT-18 protein and peptide sequences.
(A) The N-terminus of the mature CYT-18 proteins used in this study. Residues 1-32 of CYT-18 are the mt localization peptide and are cleaved upon entry into the mt matrix. Met32 in the wild-type CYT-18 construct is present as a result of translation initiation of this construct. Residues 33-61 comprise the H0 N-terminal extension. The α-helical portion of H0 is denoted. **(B)** H0-derived peptides used in this study.

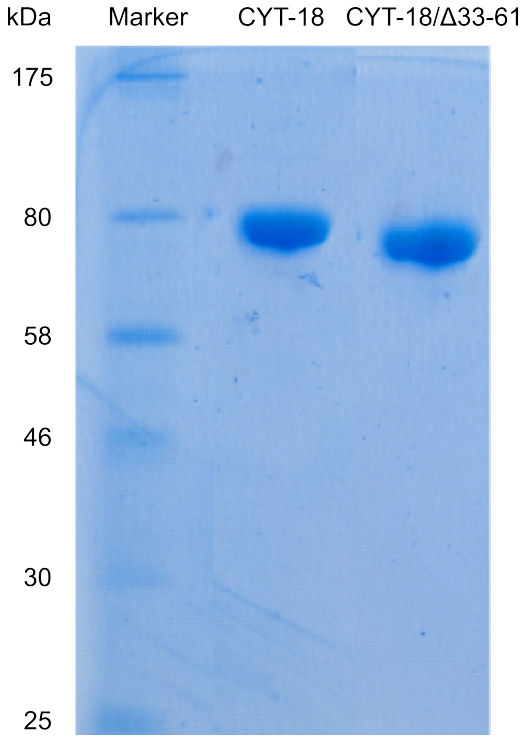

Figure 3.2 - SDS-PAGE result for purified CYT-18 and CYT-18/Δ33−61 proteins.
The purification methods for CYT-18 and CYT-18/Δ33−61 yielded > 95% pure proteins as quantified based on the Coomassie-stained 10% SDS-PAGE gel.

3.2 Tyrosyl-adenylation activity and protein stability

Tyrosyl adenylation assays were utilized to assess the activity of CYT-18/Δ33−61. Comparison of tyrosyl adenylation activity between A_{280}-normalized wild-type CYT-18 and CYT-18/Δ33−61 showed little or no reduction in activity immediately after protein purification **(Figure 3.3A)**. However, both previous studies[40] and the observations from this work indicated that the N-terminally truncated CYT-18 was less stable than the wild-type protein, presumably due to the solvent exposure of the hydrophobic H0 binding site on the core of the protein. The overall stability of the wild-type and truncated proteins were assessed by comparing their behaviors to urea denaturation/renaturation **(Figure 3.3A)**. For wild-type CYT-18, ~50% of the input protein was recovered based on A_{280} following renaturation, with the final tyrosyl-adenylation activity nearly identical to that of the non-denatured sample. For CYT-18/Δ33−61, only 15% of the total input protein was recovered with only 13% of the wild-type activity. The significant difference in both recovery and activity has suggested that H0 plays an important role in maintaining an active protein conformation.

To know if H0 is able to stabilize CYT-18/Δ33−61 during renaturation, 6-fold molar excess of H0-WT with respect to the initial concentration of CYT-18/Δ33−61 was added during renaturation. After the renaturation, CYT-18/Δ33−61 was incubated with 6-fold molar excess of H0-WT at either 37 °C or room temperature for 30 min, before its concentration was normalized with respect to the wild-type CYT-18. The tyrosyl-adenylation result **(Figure 3.3B)** shows that the addition of H0-WT has no significant effect on the renaturation of CYT-18/Δ33−61.

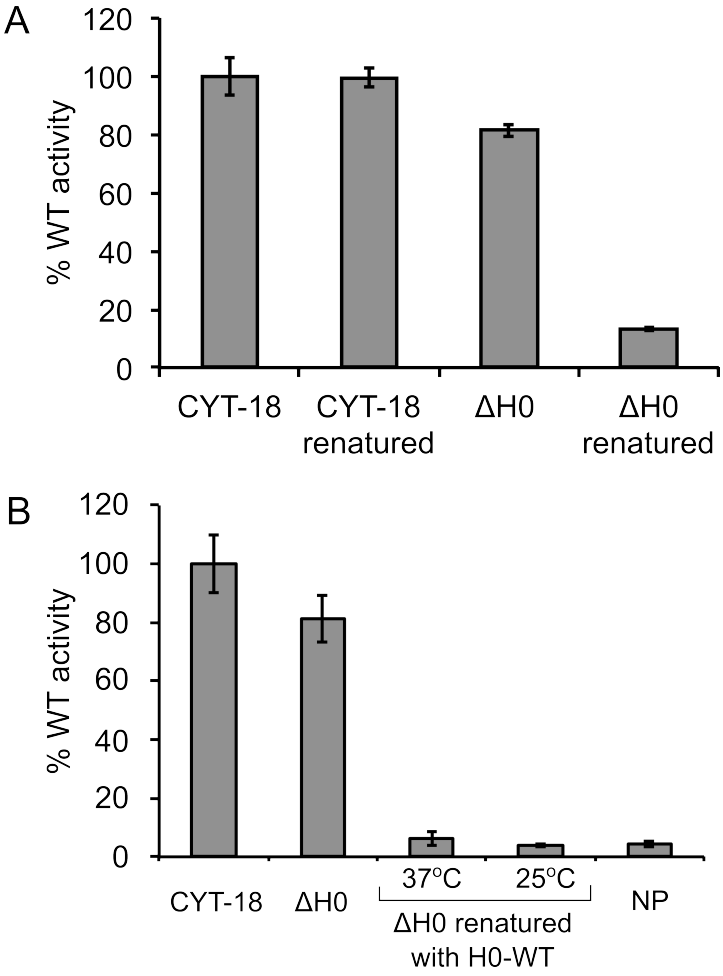

Figure 3.3 - Tyrosyl-adenylation assays for renatured proteins.
The graphs show the amount of filter-bound ^{3}H-tyrosyl-adenylate for CYT-18 and CYT-18/Δ33−61 (ΔH0) relative to wild-type CYT-18 prior to denaturation. Proteins were denatured in solution containing 8M urea and renatured by dilution and concentration without **(A)** or with **(B)** 6-fold molar excess of H0-WT. Values are the mean for 6 experiments; error bars indicate standard deviation. (NP stands for no protein)

3.3 Group I intron splicing

Based on the observed low stability of CYT-18/Δ33−61, I examined its ability to splice group I introns at three different temperatures. Consistent with previous results for other N-terminally truncated CYT-18 proteins, CYT-18/Δ33−61 has little detectable specific ND1 intron splicing at 37 °C after 60 min **(Figure 3.4A)**. However, ND1 splicing was readily detectable at 25 °C and 30 °C, though significantly decreased from the wild-type CYT-18 at these two temperatures. One major lower molecular weight RNA product was observed only in the presence of the truncated protein and was more prominent with increased temperature. This aberrant RNA product was discrete and observed from multiple protein and RNA substrate preparations but did not dependent on the addition of exogenous guanosine **(Figure 3.5)**. This result suggests that the aberrant RNA product may be the result of a specific interaction formed readily in the absence of H0 that facilitates phosphodiester backbone cleavage. Previous assays demonstrated that N-terminally truncated CYT-18 was capable of splicing the *N. crassa* mt LSU intron.[40] Consistent with these findings, CYT-18/Δ33−61 was capable of splicing the mt LSU intron at both 25 and 30 °C, though with reduced activities compared to the wild-type CYT-18 **(Figure 3.4B)**. Similar to the previous study[40], CYT-18/Δ33−61 showed detectable but significantly decreased splicing activity at 37 °C. This had been previously attributed to decreased protein stability for the N-terminal truncation and was consistent with the stability results. At all temperatures tested, there was a greater accumulation of mt LSU intermediate splicing products for both the wild-type and truncated CYT-18 in

comparison to previous studies[40]. This is likely due to the less stringent monovalent salt concentrations (50 mM vs. 100 mM) in the experiments performed.

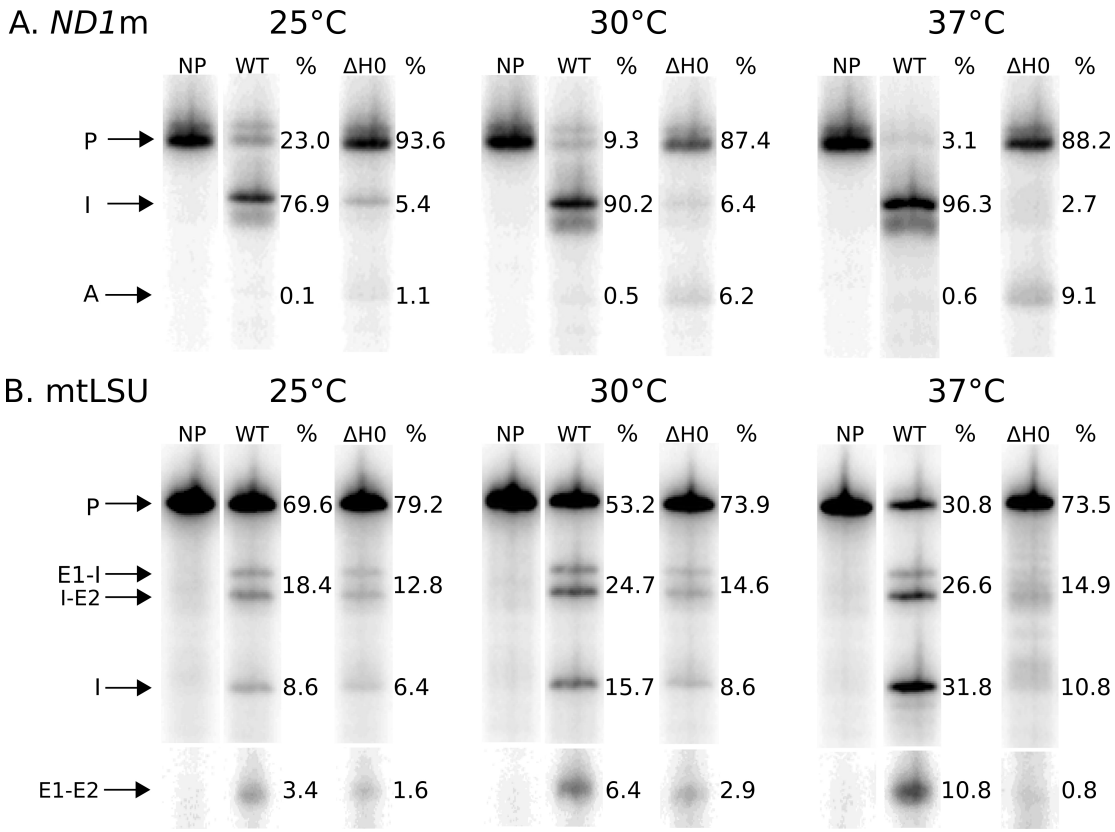

Figure 3.4 - Comparison of CYT-18 and CYT-18/Δ33−61 group I intron splicing activity.
Splicing was performed at 50 mM KCl at three temperatures for two *N. crassa* group I introns: **(A)** the ND1 intron and **(B)** the mt LSU intron. Products shown are following 60 min incubation at the given temperature. Final precursor RNA and protein dimer concentrations were 200 nM and 800 nM, respectively. A sample with no protein (NP) is shown for each temperature. Percentages of the final RNA products are shown to the right of each product. Splicing intermediates were quantified as a single band. P: Precursor RNA, I: spliced intron, E1-I: 5' exon-intron, I-E2: intron-3' exon intermediate, E1-E2: ligated exons, A: aberrant RNA product. The 14-nucleotide ligated exon product of ND1 splicing is not shown.

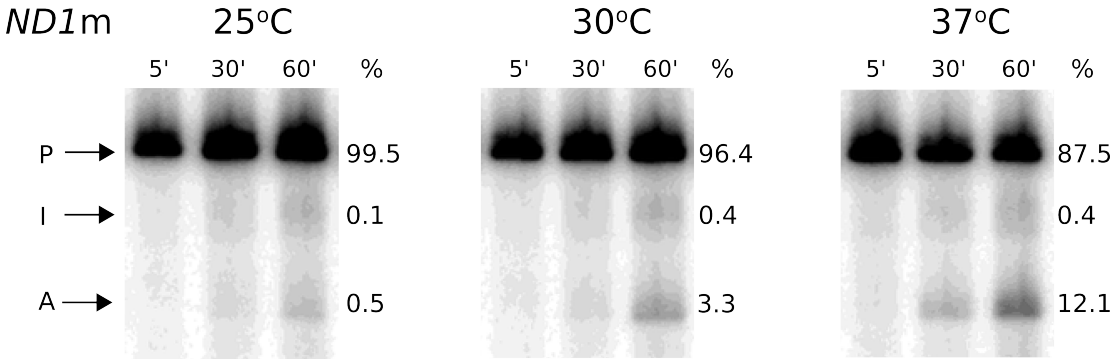

Figure 3.5 - CYT-18/Δ33−61 group I intron splicing without GTP.
200 nM ND1 intron was incubated under modified splicing conditions (no GTP) with 800 nM CYT-18/Δ33−61 (ΔH0) dimer. The incubation was performed with 50 mM KCl at three temperatures. Three time points (5', 30', 60') are shown under each temperature. Percentages of RNA products at 60' are shown to the right of each sample. P: Precursor RNA, I: spliced intron, A: aberrant RNA product.

Chapter 4: Peptide Complementation by H0-WT

4.1 Overview

The previous structural study showed that H0 is stabilized against the rest of CYT-18 primarily through two hydrophobic interactions.[39] The critical nature of these interactions was suggested by genetic experiments, which showed the involved H0 residues are either invariant or highly conserved in splicing-competent CYT-18 mutants isolated from protein libraries in which portions of H0 were partially randomized.[40] The first interaction involves Trp52 and Arg55 from the middle portion of H0, whose side chains stack with Arg95 from the protein. The second interaction involves Ile58 from the C-terminal portion of H0, which interacts with residues in H2 from the protein. To quickly examine how different H0 mutants might affect group I intron splicing, I developed a peptide complementation assay. The full-length H0 peptide (H0-WT), or derivatives (H0-37, H0-42, and H0-46), was incubated with CYT-18/Δ33−61, and the reconstituted protein was tested for intron splicing at various concentrations, temperatures, and monovalent salt concentrations.

4.2 Temperature and salt dependence

Figure 4.1 shows CYT-18/Δ33−61's ability to splice the ND1 intron in the presence of 2-fold molar excess H0-WT peptide (with respect to the protein monomer), at three different temperatures and monovalent salt concentrations. The addition of the peptide enhanced the splicing activity of the CYT-18/Δ33−61 at all temperatures, with the greatest enhancement at 30 °C and at the two lowest salt concentrations. At 25 and 30 °C, the peptide complementation assay showed maximal

activity at 50 mM KCl, while maximum splicing stimulation was observed at 25 mM KCl at 37 °C. For all temperatures tested, the amount of aberrant product was reduced in the presence of the peptide, though it was present to a greater extent at both elevated salt and temperatures. The reconstituted protein did not enhance splicing of the mt LSU intron **(Figure 4.2)**.

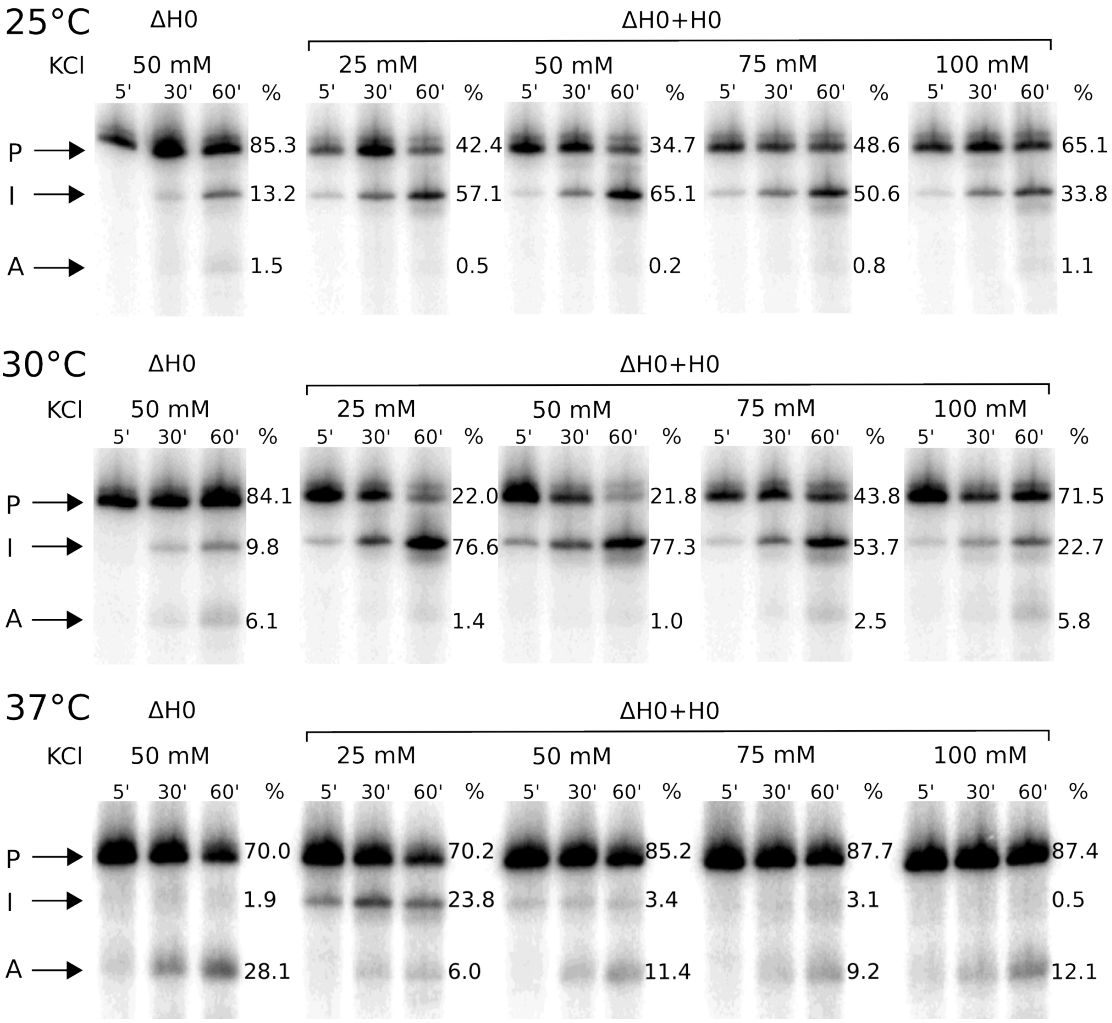

Figure 4.1 - Peptide complementation by H0-WT.
200 nM ND1 intron was incubated under described splicing conditions with 800 nM CYT-18/Δ33−61 (ΔH0) dimer alone or reconstituted with 3200 nM H0-WT peptide (ΔH0 + H0). Splicing with the reconstituted protein was performed at the three temperatures and four monovalent salt concentrations indicated. Three time points (5', 30', 60') are shown for each sample. Percentages of RNA products at 60' are shown to the right of each sample. P: Precursor RNA, I: spliced intron, A: aberrant RNA product.

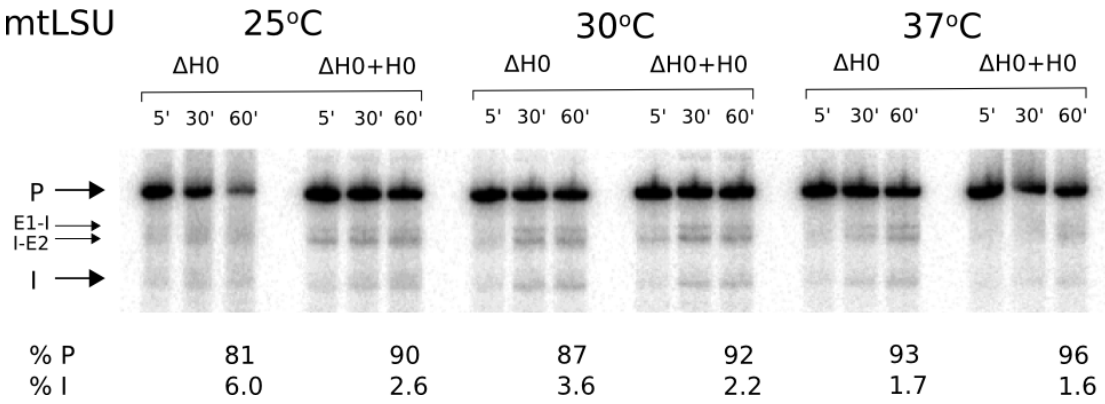

Figure 4.2 - *N. crassa* mt LSU intron splicing with H0-WT peptide complementation.
These results compare splicing of CYT-18/Δ33−61 alone or when reconstituted with 2-fold molar excess H0-WT peptide. Splicing assays were performed at 50 mM KCl as described in the main text. The percent precursor (P), and spliced intron (I) are shown for the 60' time point.

4.3 Concentration dependence

Previous studies indicated marked protein concentration dependence for CYT-18 intron splicing when N- and C-terminal truncations were used.[40] To examine if this was also true with CYT-18/Δ33−61, I performed ND1 burst splicing at two different protein concentrations with the RNA substrate in excess at 25 °C. The results are shown in **Figure 4.3**. CYT-18/Δ33−61 splicing in the absence of the H0-WT peptide was virtually identical at both the high and low protein concentrations with the precursor RNA disappearing linearly with time. Both wild-type CYT-18 and the reconstituted protein showed biphasic disappearance of the RNA precursor, with a greater extent of splicing in the initial phase at the higher protein concentration. At the lower protein concentration, the wild-type CYT-18 initial rate was 3.5 fold faster than the reconstituted protein (2.8 vs. 0.8×10^{-3} s^{-1}), but the rates were comparable (2.3 vs. 1.9×10^{-3} s^{-1}) at the higher protein concentration, indicating that the reconstituted protein at this concentration was nearly as active as the wild-type. This suggests that the reconstituted protein is functionally equivalent to the wild-type CYT-18 for splicing ND1 intron. Because the peptide/dimer ratio was maintained at 2:1, the decreased splicing at the lower protein concentration could also reflect subsaturating conditions for H0-WT binding.

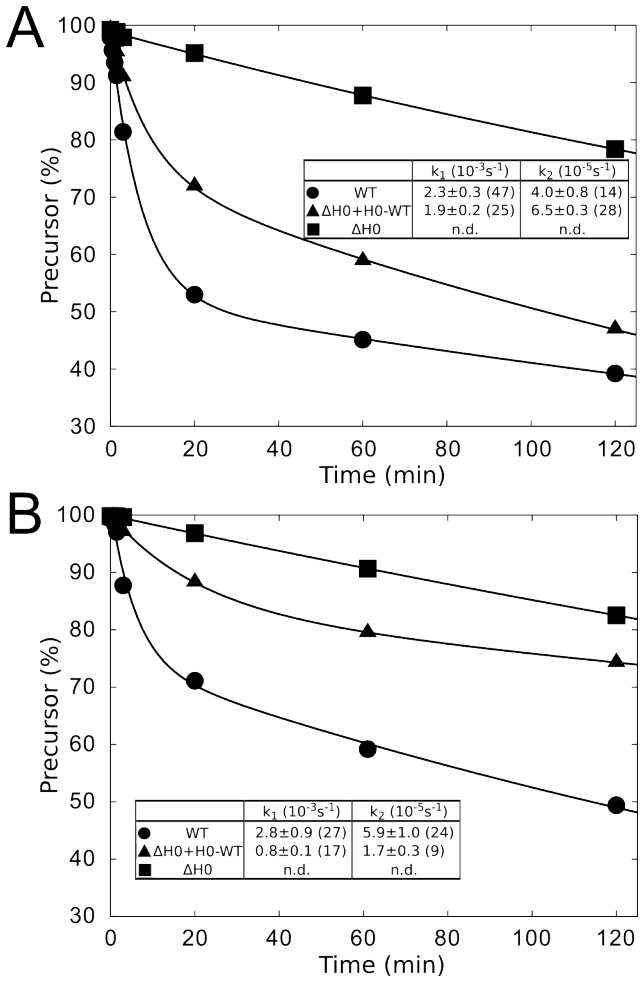

Figure 4.3 - Concentration dependence of CYT-18/Δ33−61 complementation by H0-WT.

Burst splicing reactions with precursor RNA in 2-fold molar excess to protein dimer were carried out at (A) 500 nM protein dimer and (B) 25 nM protein dimer. H0-WT peptide was maintained at 2-fold molar excess to the CYT-18/Δ33−61 (ΔH0) dimer concentration. H0-WT used in these experiments was produced recombinantly (see Chapter 2). k_{obs} for the two phases of splicing are shown with the amount of spliced product in each phase shown in parentheses.

4.4 H0 stoichiometry

The CYT-18/intron co-crystal structure suggested that the N-terminal insertions from just one of the dimer subunits were responsible for a majority of the intron contacts, with H0 from the other subunit in proximity to the intron's P5 loop.[30] Using the H0 peptide complementation assay and burst kinetic analysis, the necessary stoichiometry of H0 for intron splicing was explored. Using multiple CYT-18 protein concentrations (500, 750, and 1000 nM CYT-18 monomer), the ability of the H0-WT peptide to stimulate CYT-18/Δ33−61 splicing at ratios from 1:50 to 4:1 peptide/protein monomer was examined. **Figure 4.4** shows the percent spliced ND1 intron (relative to all RNA bands) versus the ratio of peptide to protein monomer after 10 min, a time point determined to be within the initial burst phase for the reconstituted protein. At all protein concentrations, the appearance of intron increased with the addition of peptide until reaching a peak at a peptide/monomer ratio of 1:2. Surprisingly, for 500 and 750 nM protein monomer, a drop was observed in the appearance of intron RNA at the 1:1 ratio. This decrease was not readily explainable but was observed in multiple independent experiments. In contrast, at 1000 nM CYT-18, there was a slight increase at the 1:1 ratio, though this was within error of measurements taken at 1:2 and 2:1. At all protein concentrations, the plateau was re-established at ratios of 2:1 or higher. These results indicate that single H0-WT peptide is sufficient to activate the CYT-18/Δ33−61 dimer.

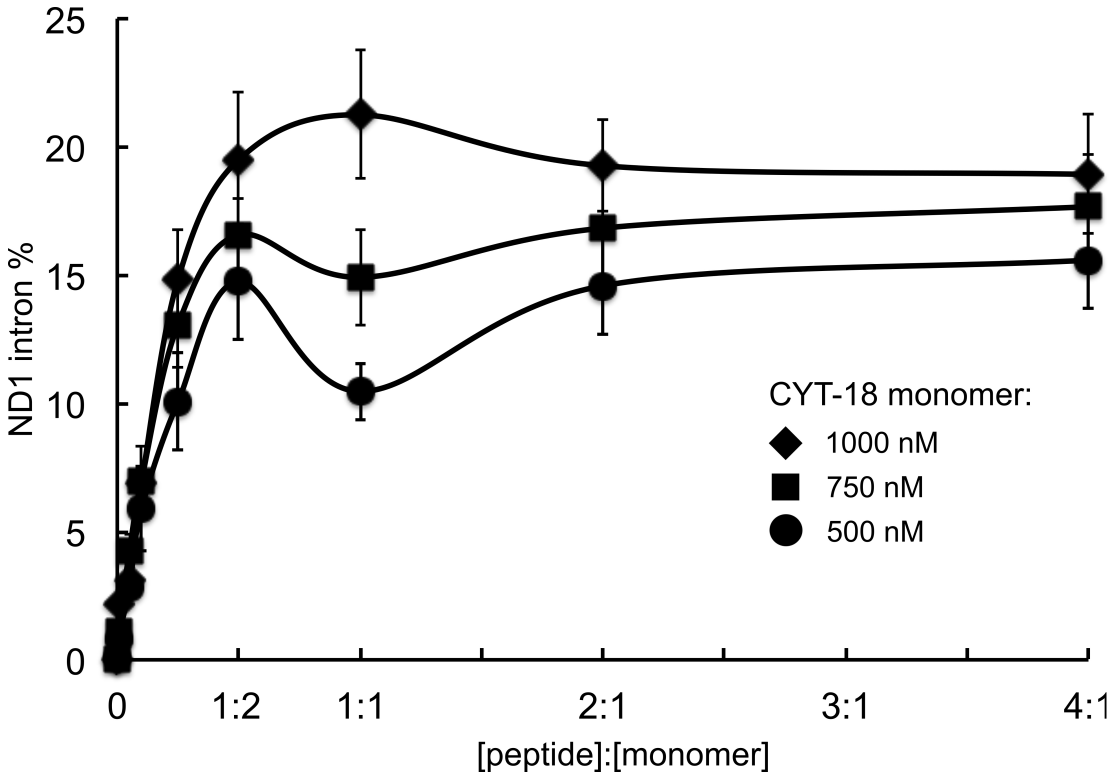

Figure 4.4 - H0 stoichiometry.
The indicated concentrations of CYT-18/Δ33−61 monomer were titrated with increasing concentration of H0-WT peptide prior to initiating the burst splicing reaction with precursor RNA in 2-fold molar excess to protein dimer. The percent intron product was determined at the 10 min time point and plotted against the molar ratio of peptide to CYT-18/Δ33−61 monomer. Points are the mean from three independent experiments. Error bars are standard deviations.

Chapter 5: The Five N-Terminal H0 Residues Are Required for Efficient Intron Splicing

5.1 Truncated H0 peptides fail to trans-activate splicing

The H0 peptide complementation assay was developed to provide a rapid way of exploring how modified H0 peptides can impact group I intron splicing. Three different N-terminally truncated H0 peptides (H0-37, H0-42, and H0-46; **Figure 3.1B**) were examined. H0-WT and all three truncated peptides had similar spectra in circular dichroism measurements **(Figure 5.1)**, indicating that there were no major structural differences in solution. Surprisingly, when used in the peptide complementation assay, none of the truncated peptides were capable of significantly stimulating CYT-18/Δ33−61's ND1 intron splicing activity **(Figure 5.2A)**. The lack of splicing could be the result of the peptides not binding to the truncated protein or their inability to productively contact the intron RNA when bound to CYT-18/Δ33−61. Competition assays using 3-fold molar excess of the truncated peptides to H0-WT revealed little (H0-42) or no (H0-37, H0-46) reduction in H0-WT's ability to *trans*-activate CYT-18/Δ33−61's splicing activity **(Figure 5.2B)**.

The inability for even the shortest N-terminal peptide truncations to bind or stimulate splicing in the peptide complementation assay indicated for the first time that these residues might have an important functional role in intron splicing. To compare how short N-terminal truncation might differ between the peptide complementation experiments and a truncated recombinant CYT-18, CYT-18/Δ33−37 protein was constructed that lacks just the first five amino acids. This

protein did not have the stability issues observed with CYT-18/Δ33−61 and behaved identically to wild-type CYT-18 in tyrosyl adenylation assays **(Figure 5.3)**. However, consistent with observations from the peptide complementation assays, this N-terminally truncated protein had significantly reduced splicing activity for the ND1 intron at 50 mM KCl at all three temperatures tested **(Figure 5.4A)**. The aberrant splicing product was also present at levels comparable to CYT-18/Δ32−61 at 37 °C. Interestingly, the CYT-18/Δ33−37 also showed reduced splicing activity for the mt LSU intron when compared to wild-type CYT-18 **(Figure 5.4B)**. Together, these results indicate that the N-terminal most residues of CYT-18 play a role in splicing both the ND1 and mt LSU introns.

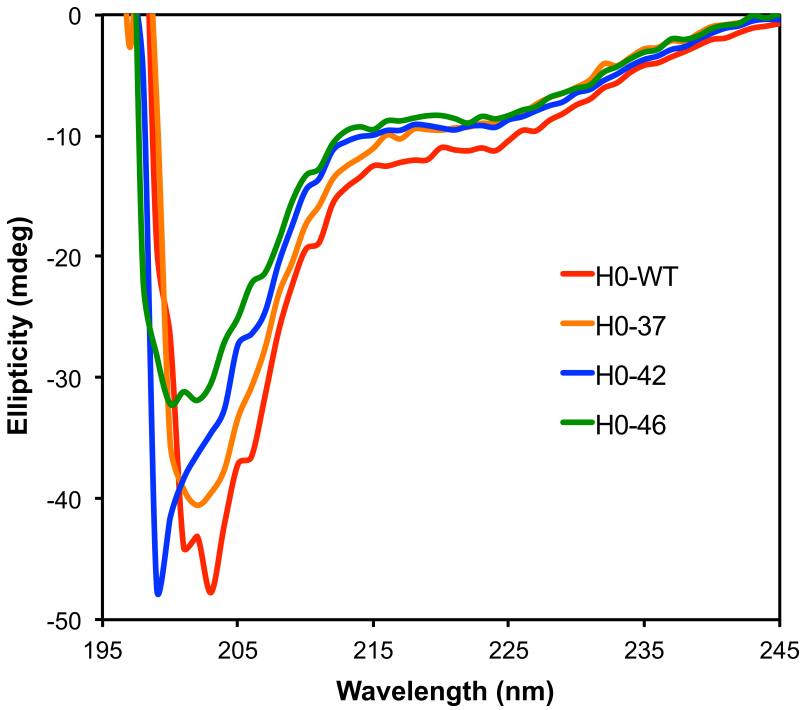

Figure 5.1 - Background-subtracted circular dichroism spectra of the peptides used in this study.
Circular dichroism experiments were done with H0-WT and truncated H0 peptides in 10 mM Tris-HCl (pH 7.5) and 10 mM KCl. The peptide concentration was adjusted to 12 μM based on A_{280} and analyzed by Jasco J-810 spectropolarimeter. The negative ellipicity at ~205 and 225 nm are indicative of the presence of α-helices.

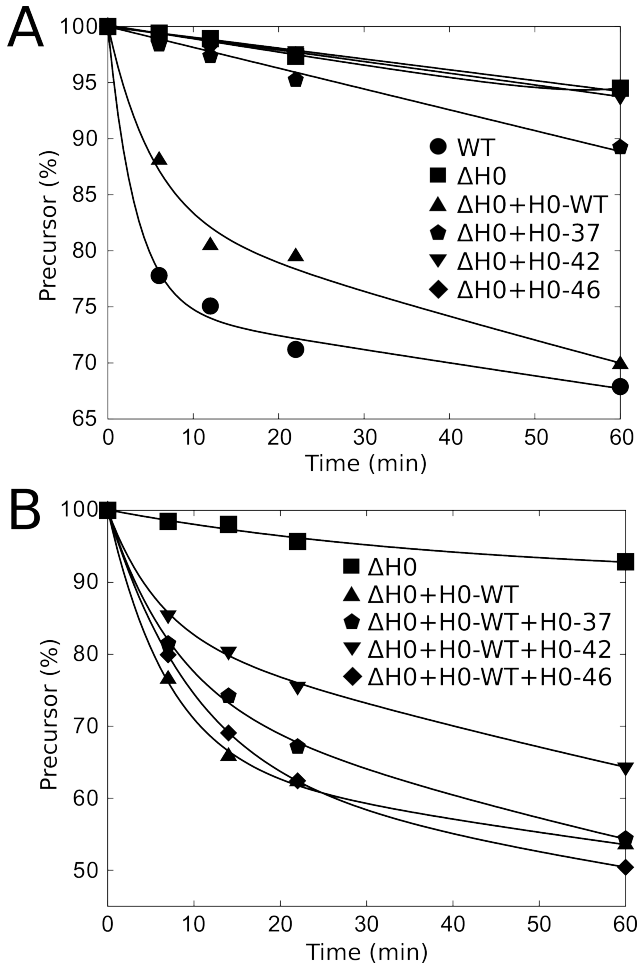

Figure 5.2 - Peptide complementation with truncated H0 peptides.
(A) Burst splicing time courses using 500 nM dimeric CYT-18 (WT), CYT-18/Δ33−61 (ΔH0) alone, and with equimolar H0 peptides to protein monomer. **(B)** Truncated peptide competition experiments. 500 nM CYT-18/Δ33−61 dimer was incubated with peptide mixtures containing 1 μM H0-WT and 3 μM N-terminally truncated H0 peptide. H0-WT used in these experiments was produced recombinantly (see Chapter 2).

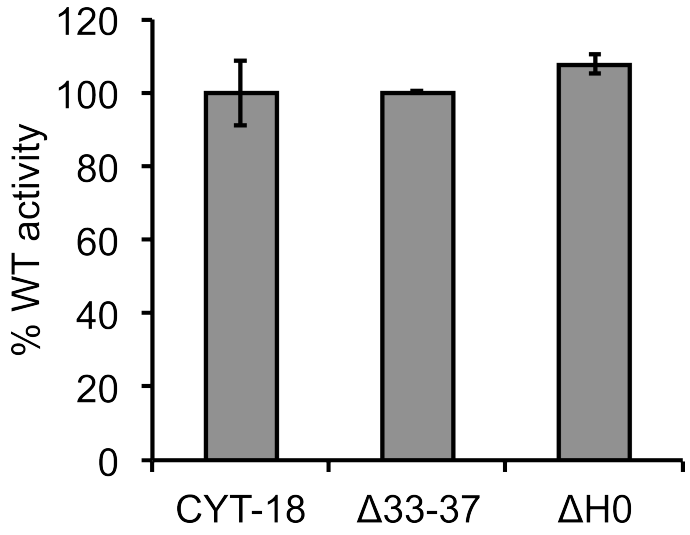

Figure 5.3 - Tyrosyl-adenylation assays for CYT-18/Δ33−37.
The graph shows the amount of filter-bound ^{3}H-tyrosyl-adenylate for CYT-18, CYT-18/Δ33-37 (Δ33−37), and CYT-18/Δ33−61 (ΔH0). Values are the mean for 6 experiments; error bars indicate standard deviation.

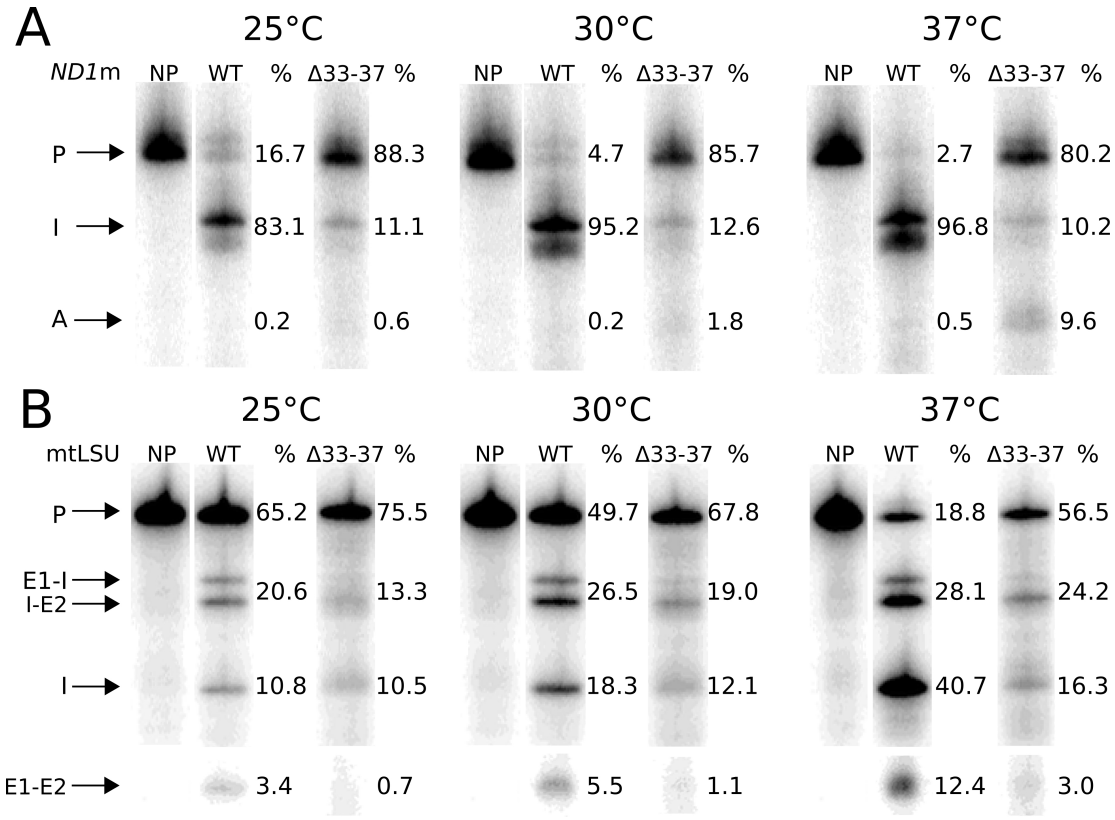

Figure 5.4 - CYT-18/Δ33−37 group I intron splicing.
Splicing was performed at 50 mM KCl at three temperatures for two *N. crassa* group I introns: **(A)** the ND1 intron and **(B)** the mt LSU intron. All products shown are following 60 min incubation at the given temperature. Products are labeled and quantified as in **Figure 3.4**.

5.2 RNA equilibrium binding assay

In order to know if the *trans*-activation of CYT-18/Δ33−61's splicing activity by H0 complementation is due to an improved protein/RNA binding, and to know if the five N-terminal-most residues are important to CYT-18/RNA binding, I performed *N. crassa* ND1 intron RNA equilibrium binding assay with the reconstituted protein of CYT-18/Δ33−61 and H0 peptides (2-fold molar excess with respect to the protein monomer), and CYT-18/Δ33−37 **(Figure 5.5)**.

The normalized binding percentage (with respect to wild-type CYT-18) has improved from 13% for CYT-18/Δ33−61 alone to 40% for the reconstituted protein (CYT-18/Δ33−61 and H0-WT). Since the improvement in protein/RNA binding is ~25% lower than the improvement in ND1 splicing observed in the peptide complementation by H0-WT (52% increase under the same condition), I reasoned that apart from assisting in protein/RNA binding, H0-WT also stabilizes CYT-18/Δ33−61 by minimizing protein aggregation caused by non-native hydrophobic interactions. In agreement with the other peptide complementation results, the N-terminally truncated H0 peptides all failed to significantly improve the ND1 intron binding of CYT-18/Δ33−61. The failure to improve RNA binding accounts for the inability of the N-terminally truncated H0 peptides to *trans*-activate CYT-18/Δ33−61's ND1 splicing activity. However, CYT-18/Δ33−37 showed a similar RNA binding percentage as the wild-type CYT-18, suggesting that the five N-terminal-most residues are dispensable for CYT-18/ND1 intron binding. The RNA equilibrium binding assays provide information on how peptide complementation by H0-WT *trans*-activates the splicing activity of CYT-18/Δ33−61. The *trans*-activation

is attributed to the improvement of protein/RNA binding and possibly the improved stability of the protein.

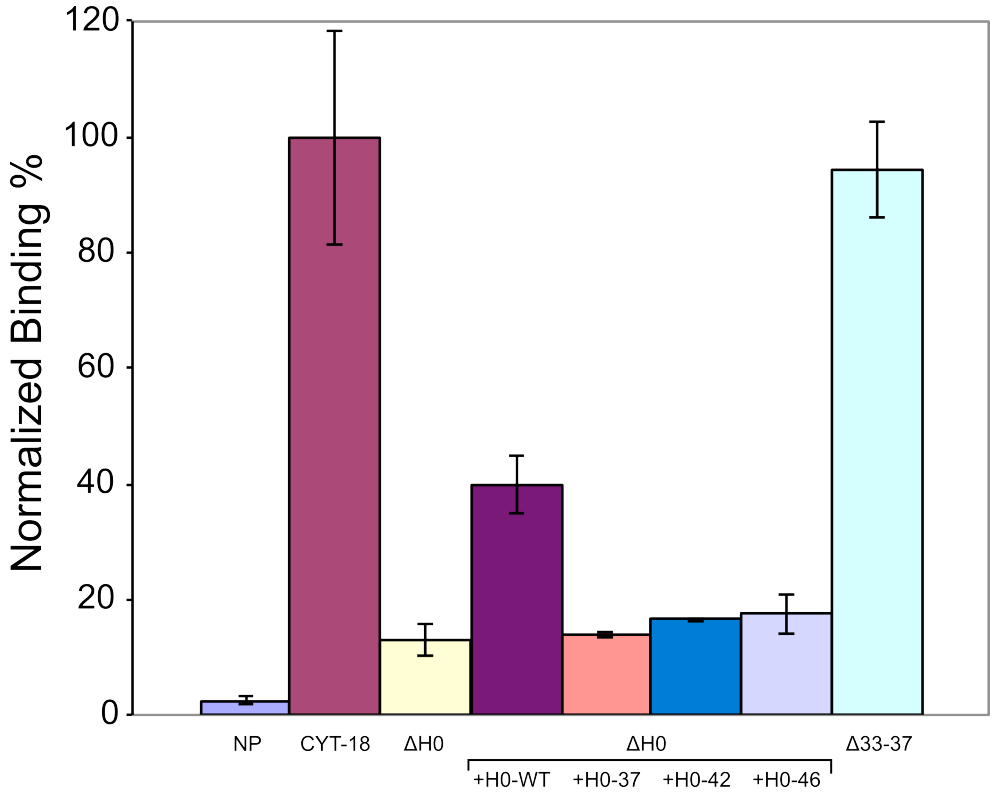

Figure 5.5 - RNA equilibrium binding assay for *N. crassa* ND1 intron
The normalized binding percentages indicate the ratios of protein-bound ^{32}P RNA out of the input ^{32}P RNA with respect to the wild-type CYT-18. (NP stands for no protein)

5.3 Crystal structure re-evaluation

The importance of H0's five N-terminal-most residues for ND1 splicing in the context of both the full-length protein and the peptide complementation splicing led me to re-examine the CYT-18/Δ424−669 crystal structure for structural clues to their function. Despite weak electron density, these residues were successfully built using the original data by my laboratory, now guided in part by the contiguous backbone density in the co-crystal structure[15] (**Figure 5.6** and **Figure 5.7A**). Along with the addition of the N-terminal residues, several side chains were successful added, which had been omitted from the H0 helix (Glu47, Glu49) resulting in an overall reduction in R_{free} and improved model geometry **(Table 5.1)**. The backbone density was reasonably well-defined for residues 33−38, while the side chain density varied. Significantly, Arg34 and Arg35 had the most well-defined side chains. The refined structure showed that Arg35 makes a potential salt bridge with Glu296 from Ins2 (**Figure 5.6B** and **Figure 5.7B**) and Arg34 makes a potential salt bridge with Glu49 from the H0 α-helix while also making potential hydrogen bonding contacts with Asn46 **(Figure 5.6C)**.

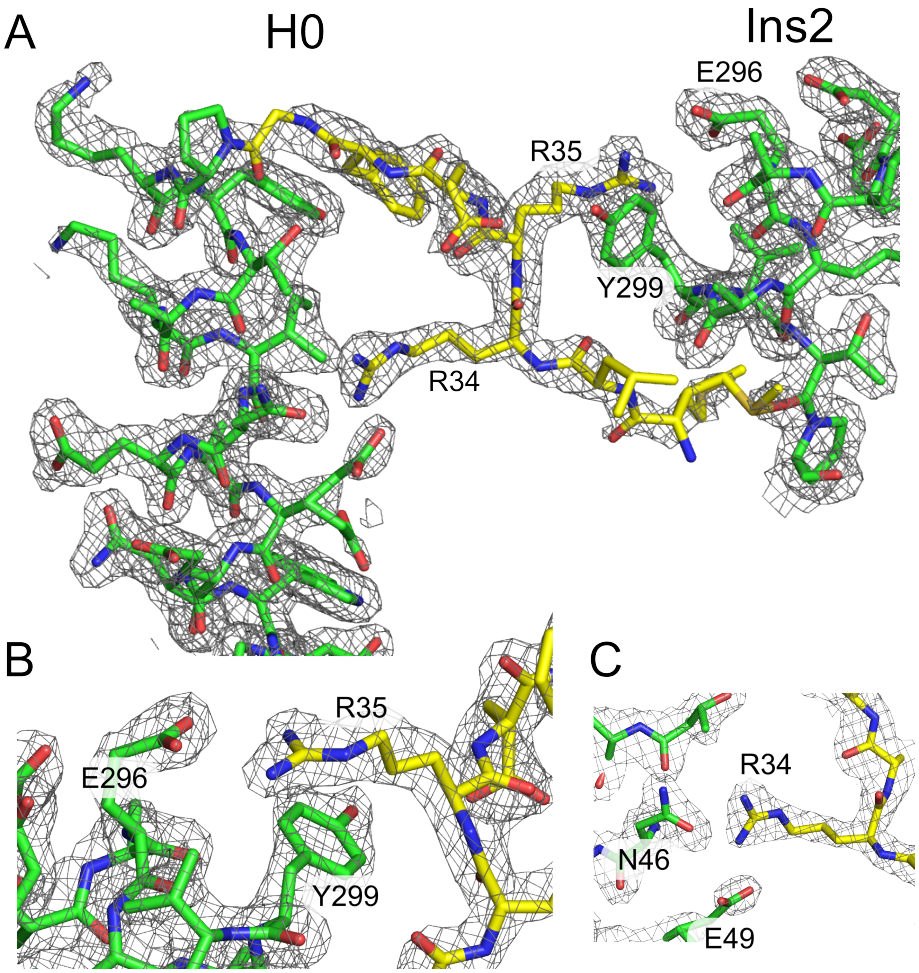

Figure 5.6 - Structural evidence for ionic interactions by H0 N-terminal residues. **(A)** $2m|F_o| - D|F_c|$ electron density contoured at 1.0σ around H0 and Ins2 amino acids. H0 residues shown in yellow are newly built residues using the original CYT-18/Δ424−669 crystal structure data. **(B)** and **(C)** show the potential ionic interactions between Arg35 with Glu296 of Ins2, and Arg34 and Glu49 of H0, respectively.

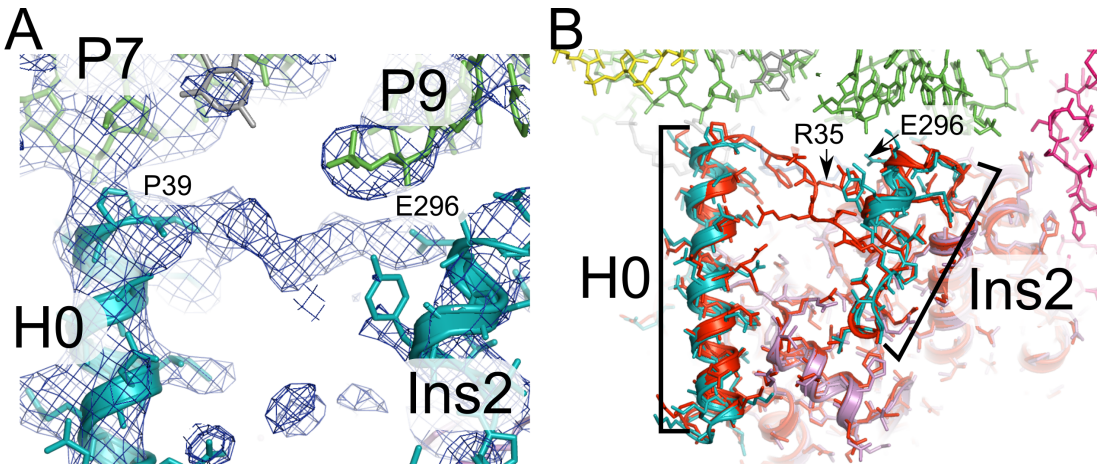

Figure 5.7 - CYT-18 co-crystal structure.
(A) Contiguous electron density between H0 and Ins2 (cyan). RNA structural elements (green, grey) in proximity to H0 and Insertion 2 (P7, P9) are labeled. **(B)** Superposition of the CYT-18 co-crystal structure and the newly refined CYT-18/Δ424−669 structure (red).

Table 5.1 - Comparative refinement statistics

	Original refinement	New refinement
Refinement		
Resolution (Å)	20-1.95	58.6-1.95
R_{work} / R_{free}	17.4/23.5	16.7/21.1
R.m.s deviations		
Bond lengths (Å)	0.018	0.007
Bond angles (°)	1.621	1.127
PDBID	1Y42	4OJM

Chapter 6: Summary and Discussion

6.1 Only one H0 insertion of the CYT-18 homodimer is required for splicing

The peptide complementation assay developed has allowed me to address several major questions not fully explained by previous biochemical or structural information. First, this work has been able to address if both H0 insertions of the homodimer are required for splicing. Understanding the different roles of the two CYT-18 subunits in splicing has been challenging due to the difficulty of creating and purifying heterodimeric CYT-18. The CYT-18/Twort intron co-crystal structure established that H0 from one subunit was responsible for contacting the intron RNA directly, but the close proximity of H0 from the other subunit to the P5 region of the RNA,[15] as well as site-directly hydroxyl cleavage data that placed H0 residues near P5[39] suggested that H0 insertions from both subunits may be involved in splicing. By controlling the relative concentrations of the H0 peptide and CYT-18 protein, this work demonstrated over a range of protein and peptide concentrations that ND1 splicing reaches a plateau when a maximum of 50% of the H0 binding site could be occupied. This strongly suggests that only a single H0 peptide is necessary for productive splicing. If the second H0 contacts the intron RNA, these interactions are not required for establishing a splicing-active intron conformation. It remains unclear why a drop in splicing activity was observed at equimolar concentrations of peptide to protein monomer at certain protein concentrations, though this may be related to concentration dependence observed in **Figure 4.3**. The drop in activity might imply negative cooperativity, though it is not clear why the activity would increase with the addition of more peptide. One possibility may be that the process of binding of the

second peptide induces a local asymmetry in the protein dimer that negatively affects splicing. This subtle negative cooperativity could therefore be observed most prominently at or near conditions of peptide saturation. CYT-18 and bacterial TyrRS's all display half-of-sites reactivity in tRNA charging, which is thought to be an extreme case of negative cooperativity induced by dimer asymmetry.[42]

6.2 CYT-18's N-terminal-most residues play an important role in intron splicing

The peptide complementation assay has also provided the first evidence that the N-terminal-most residues play an important role in intron splicing. The CYT-18/Δ424−669 crystal structure suggested that a majority of the contacts between H0 and the rest of CYT-18 were through hydrophobic interactions.[39] Based on this information, I reasoned that the N-terminally truncated H0 peptides that retained those hydrophobic interactions would bind to CYT-18/Δ33−61 nearly as well as the H0-WT peptide. Because only the N-terminus of H0' s α-helical region was found to contact the Twort intron in the co-crystal structure, the initial anticipation was that only peptides shortened beyond Pro39 would fail to complement splicing and that these peptides might function as competitive inhibitors of H0-WT complementation. The inability of the truncated peptides, including H0-37 which retained the entire α-helical sequence, to efficiently complement splicing or compete with H0-WT for complementation is consistent with the truncated peptides being unable to efficiently bind the protein at the H0 binding site, despite the peptides having all of the hydrophobic residues that make up a bulk of the interaction surface with the TyrRS core. Most simply, these results suggest that the five N-terminal residues that are

present in H0-WT but absent in H0-37 must interact with either another part of the protein or the intron RNA to enhance peptide binding.

Splicing with the CYT-18/Δ33−37 protein showed significantly reduced splicing activity for both the ND1 and mt LSU introns, indicating that these first five residues are important for splicing in the context of the full-length protein and not just for peptide binding in the complementation assay. Further, CYT-18/Δ33−61 and CYT-18/Δ33−37 showed similar reduced mt LSU splicing activity in comparison to wild-type CYT-18 at all temperatures tested. Because CYT-18/Δ33−37 did not exhibit the same issues with solubility, the decreased mt LSU splicing activity for these and other N-terminal truncations is not likely due entirely to decreased protein stability as was previously ascribed.[40]

6.3 Key ionic interactions are suggested between H0 residues and Ins2

The peptide complementation assay has also provided initial evidence for how these residues may be functioning in the full-length protein. The H0-WT peptide showed a decreased ability to complement splicing at elevated monovalent salt and temperature. The CYT-18/group I intron interaction itself is salt dependent,[25, 27, 30] and the salt-dependent complementation could simply reflect a decrease in intron affinity. However, previous studies indicated that binding and splicing were reduced only at KCl concentrations greater than 100 mM at 37 °C.[25, 27] Because this is a tripartite system, the decrease in activity may also be due to decreased peptide affinity at higher salt and temperature, implicating ionic interactions.

Several other lines of analysis suggest that charged residues in the H0 N-terminus and Ins2 are being involved in ionic interactions. Most directly, this ionic

interaction in the CYT-18/Δ424−669 crystal structure has been successfully visualized. The missing N-terminal residues were successfully built to show that Arg35 makes a potential salt bridge with Glu296 from Ins2. Previous biochemical data had implicated Glu296 and surrounding residues as being important in intron splicing. A short Ins2 deletion mutant that removed Glu296 inhibited ND1 intron splicing activity.[39] The importance of this interaction is also evident from sequence analysis of Pezizomycotina mt TyrRS's[30]. Arg35 is highly conserved in the Pezizomycotina mt TyrRS's (15 of 18 species). One of these exceptions, *Stagansopora nodorum*, is believed to have lost its intron splicing activity[30, 43], while another, *Podopspora anserina*, contains tandem lysine residues just N-terminal of the Arg34 position. Only the mt TyrRS from *Magnaporthe grisea* appears to lack basic residues at the H0 N-terminus[30]. Previous sequence analysis revealed that Ins2 of Pezizomycotina mt TyrRS's lacked significant positional sequence conservation, but compositionally these insertions contained a large number of prolines and acidic residues.[30] Overall, these mt TyrRS's average 4 acidic residues in this 18 amino acid insertion, though notably the *M. grisea* mt TyrRS contains the fewest number of acidic residues with only two. The conserved charge distribution between the H0 N-terminus and Ins2 suggests an evolutionary conservation of ionic interactions between H0 and Ins2.

6.4 H0 serves as an important structural link connecting the N-terminal splicing insertions of CYT-18.

The CYT-18/group I intron complex has been a unique system for understanding how small protein adaptations can evolve to recognize distinct but

related RNA substrates.[30, 39, 44] My study largely supports these previous results but hints at greater complexity. Previous structural information on CYT-18 showed that H0 makes side chain contacts with Ins1. This study establishes that H0 also interacts with Ins2, placing H0 in contact with both of the other N-terminal splicing insertions. It had been previously suggested that the role of H0 in splicing the mt LSU intron was primarily to stabilize another region of the protein that directly contacted the intron RNA.[40] This analysis can be explained by my results that suggest that the salt bridge between H0' s N-terminal residues and Ins2 may be important for establishing the relative orientation of H0 and Ins2 during splicing. Thus, even if H0 does not directly contact some group I introns, it may still be important in helping to stabilize or position Ins1 and Ins2.

The development of a peptide complementation assay has allowed me to gain further insight into H0' s role in group I intron splicing. My results indicate that H0 serves as an important structural link that connects the N-terminal splicing insertions of CYT-18. It has been previously suggested that the highly specific structural features of the mt TyrRS splicing adaptations make them potentially unique targets for the development of antifungal drugs for Pezizomycotina species[30] such as *Histoplasma capsulatum*, *Coccidiodies sp.*, and *Aspergillus sp.* This study has elucidated a new role for H0' s N-terminal residues, further highlighting it as a potentially targetable feature for drug development. Importantly, this H0 peptide complementation has been demonstrated capable of uncovering important features required for group I intron splicing activity. This assay will likely become a key tool

in assessing small molecule inhibitors that could target mt TyrRS N-terminal insertions.

6.5 Contributions to present knowledge and future implications

The peptide complementation assay has allowed me to address several major questions not fully explained by previous studies. First, this work has been able to address if both H0 insertions of the homodimer are required for splicing. I have demonstrated only one H0 insertion of CYT-18 is required for productive splicing. This assay has also provided the first evidence that the N-terminal-most residues play an important role in intron splicing, which led to the finding of H0's new role as a structural link connecting all three N-terminal insertions to help maintain their relative positions for productive intron binding.

Since the expression of many fungal mt genes require proper splicing of group I introns, suppressed group I intron splicing of these genes will result in a lack of mature RNAs that leads to a suppressed mt gene expression. The insufficient mt gene expression will further suppress cellular respiration, which exerts detrimental effects on the obligate aerobic fungal organism. For instance, in the mt of *N. crassa*, failure to splice ND1 intron will suppress gene expression of NADH dehydrogenase, causing a suppressed oxidation phosphorylation in mt. In addition, failure to splice mt LSU intron will cause a suppressed mt ribosome assembly, largely affecting the mt protein translation.

Like other mt proteins that are expressed from nuclear genes, CYT-18 is translated in cytosol and retained unfolded with the aid of the cytosolic chaperones. Guided by the N-terminal mt targeting sequence, CYT-18 is transported into the mt

matrix. After cleavage of the N-terminal mt targeting sequence, the unfolded CYT-18 folds presumably with aid of the mt chaperones. The partially folded CYT-18 protein during the folding process can be a good candidate for antifungal drug target. Since H0 becomes the N-terminal extension of CYT-18 following the cleavage of the N-terminal mt targeting sequence, it presumably folds in last after the mt TyrRS core is fully folded. Based on these analyses and that H0 in a fully folded CYT-18 is important to the group I intron splicing, researchers can potentially use small molecule drugs that could competitively bind to the H0 binding site on the mt TyrRS core during the last step of protein folding. By competitively and exclusively occupying the H0 binding site and prohibiting formation of a completely folded and splicing-competent CYT-18 with a properly folded H0, the small molecule drugs can suppress the mt group I intron splicing and essential mt gene expression, which will suppress the cellular respiration and exert detrimental effects to the obligate aerobic fungal organism.

Therefore, a major future direction of this work is to use the developed peptide complementation assay as a key tool in assessing small molecule inhibitors that could target mt TyrRS N-terminal insertions. By rapidly screening numerous small molecule inhibitors from the drug libraries built by in silico screening and yeast cell biological experiments, researchers should be able to quickly discover potent drug candidates that are featured by high and specific binding affinity to the H0 binding site.

PART II: THREE-DIMENSIONAL DNA CRYSTALS AS VEHICLES FOR BIOCATALYSIS

Chapter 7: Introduction

7.1 Goals of DNA nanotechnology

DNA has proved to be a successful material for the self-assembly of nano-scale structures in two and three dimensions because of its inherent programmability and predictable structural features.[45-54] One of the original[55] and ongoing goals of the DNA nanotechnology field has been the rational design of periodic three-dimensional DNA arrays, or crystals.[56, 57] DNA crystals have been envisioned as self-assembling porous solids that could be used as molecular scaffolds for the structure determination of proteins, as templates for 3D molecular electronics,[58] or as zeolite-like materials for separations and catalysis.[59] Such crystals were originally designed to serve as 3D scaffolds that tether molecules of a guest protein at specific locations and orientations, thus the protein structure could be determined as part of the DNA lattice.[55] If implemented correctly, this approach could bypass the crystallization problem for difficult-to-crystallize, but pharmaceutically significant proteins.

7.2 Rationally designed 3D DNA crystals with a non-Watson-Crick motif

The DNA crystals used in this study originate from a previously reported 3D DNA crystal structure.[60] The original structure was the first reported continuously base-paired 3D DNA lattice, which was self-assembled into a 3D crystalline array from a DNA 13-mer oligonucleotide (PDB ID: 1P1Y).[60] In contrast to other DNA oligonucleotide structures, it is composed of both Watson-Crick and non-canonical

base-parings.[60] The non-canonical base-pairings function as branches connecting the linear Watson-Crick duplexes into a periodic 3D assembly. This non-Watson-Crick motif was demonstrated to be predictable and could be used to rationally design DNA crystals with expanded lattice dimensions that self-assemble in the presence of divalent cations.[60]

The DNA crystals **(Figure 7.1A)** used in this study were designed to have expanded solvent channels that run through the length of the crystals.[60] Down the six-fold crystallographic symmetry axis, these channels are ~9 nm in diameter **(Figure 7.1B)** and previous work[61] showed that proteins with molecular weights (MW) of 14-45 kDa could be incorporated into these channels, while larger proteins were excluded from the crystal interior. Based on these observations, development of a DNA crystal-based enzyme container for biocatalysis is possible. The activity of enzymes encapsulated within the crystals' solvent channels can be examined, while the activity from any enzyme free in solution is inhibited by recombinant enzyme inhibitor (MW > 45 kDa) that is excluded from the crystal interior. This study shows that protein enzymes encapsulated in the solvent channels of a DNA crystal are capable of performing catalysis. The kinetic properties of these encapsulated enzymes have features consistent with other immobilized enzymes,[62-67] and represent a solid-state biomolecular catalyst composed entirely of biological molecules.

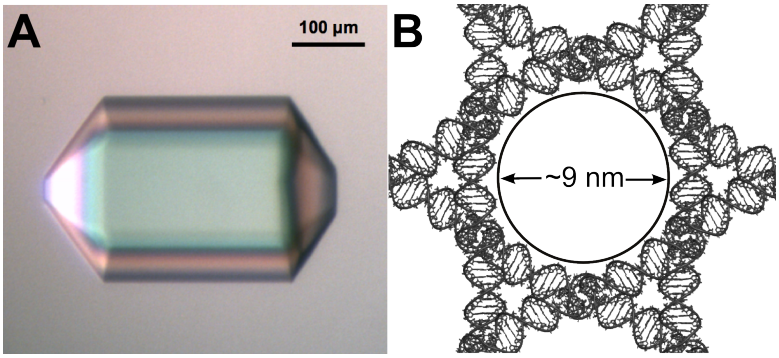

Figure 7.1 - Three-dimensional DNA crystals.
(A) Image of a representative crystal used in this study from light microscopy. **(B)** Crystals contain channels ~9 nm in projection that run down the six-fold symmetry axis.[60]

7.3 Immobilization methods of enzymes and mass-transfer effects

Aiming at improved stability and easiness of separation/recycling from the reaction media, numerous immobilization methods of enzymes have been developed following six decades of extensive exploration.[64, 68, 69] The immobilization methods range from binding to carrier to cross-linked enzyme crystals or lyophilized powders.[64, 69] However, for most of these methods, physical restriction of the enzyme mobility caused by enzyme immobilization affects the solute mobility, which is referred to as mass-transfer effect. Among the immobilization methods of enzymes, most, if not all are subject to mass-transfer effects, which generate substrate or pH gradients that change the enzymatic rates. Since the 3D DNA crystals used in this study also restrict the mobility of enzymes by encapsulation, the crystal-encapsulated enzymes would very likely show enzymatic kinetics different from aqueous enzyme systems that are free of diffusional limitations.

Chapter 8: Experimental Procedures

8.1 Expression and purification of recombinant MBP-tagged RNase inhibitor

The porcine RNase inhibitor open reading frame[70] (a generous gift of Prof. Jan Hofsteenge, Friedrich Miescher Institute, Basel) was cloned into vector pMAL-C2T, verified by sequencing using malE primer, and expressed using autoinduction in *E. coli* HMS174(DE3) cell. The MBP fusion protein was purified by amylose affinity chromatography. Inhibitor activity was assayed in the following mixture with a Perkin-Elmer fluorometer (λ_{excit} = 478 nm; λ_{emis} = 522 nm): 0.63 μM RNA substrate; 0-200 μM RNase A; 10 mM sodium cacodylate (NaCaco) pH 7.0; 120 mM magnesium formate ($Mg(HCO_2)_2$); and 50 mM lithium chloride (LiCl).

8.2 DNA crystallization

Individual DNA strands **(Figure 8.1)** were synthesized by standard phosphoramidite chemistry, purified by denaturing polyacrylamide electrophoresis followed by electroelution, desalted by using dialysis, and concentrated in a vacuum concentrator. The assembly strand and spacer strand were mixed in a 1:1.1 ratio and the final concentrations were adjusted to 0.21 mM. Crystals were grown in sitting-drop vapor diffusion trays by mixing 2 μL of the DNA solution with 2 μL of the well solution (120 mM $Mg(HCO_2)_2$, 50 mM LiCl, and 10% 2-methyl-2-4-pentanediol) and incubating at 37 °C overnight before gradually cooling to 22 °C at a rate of 1 °C/15 min. Crystals appeared in 2-4 days and reached a maximum length of 0.8 mm.

EX11	5'-**GGA CAG CTG CTG ACT GAT TGG GAG**-3'
EET11	5'-**CAA TCA GTC AG**-3'
EX11rodtrial1	5'-**GGA CAG CTG CTG ACT GAT TCG GAG**-3'
EET11rodtrial1	5'-**GAA TCA GTC AG**-3'

Figure 8.1 – Sequences for the DNA oligonucleotides used in this study.
Crystals generated from EX11 (assembly strand) and EET11 (spacer strand) were used for some of the direct fluorometry assay described below. Crystals generated from EX11rodtrial1 (assembly strand) and EET11rodtrial1 (spacer strand) were used for the rest of study.

8.3 RNase A incorporation and protein coating of a DNA crystal

RNase A was incorporated through diffusing by transferring a single DNA crystal into RNase A soaking buffer (44 mg/mL bovine pancreatic RNase A, 10 mM NaCaco pH 7.0, 120 mM $Mg(HCO_2)_2$, and 50 mM LiCl) and incubating at 4 °C for 4 days. Protein coating was performed after the RNase A-infused DNA crystal was washed by soaking twice in 200 µL MFJ buffer (10 mM NaCaco pH 7.0, 120 mM $Mg(HCO_2)_2$, and 50 mM LiCl), followed by removal of 100 µL of solution and addition of 100 µL fresh MFJ buffer three times. For coated crystals, the washed RNase A-infused DNA crystal was transferred into hen egg-white lysozyme soaking buffer (30 mg/mL lysozyme, 10 mM NaCaco pH 7.0, 120 mM $Mg(HCO_2)_2$, and 50 mM LiCl) and incubated for 5 min. The crystal was then transferred to cross-linking buffer (2% fresh glutaraldehyde, 10 mM NaCaco, pH 7.0, 120 mM $Mg(HCO_2)_2$, and 50 mM LiCl) and incubated for 30 min. The crystal was washed again and incubated with RNase inhibitor or MBP-RNase inhibitor for at least 10 min before the activity assay. All activity assays also included excessive MBP-RNase inhibitor in the reaction conditions. All routine washing and protein coating steps were performed at room temperature.

8.4 Fluorescence measurements and reusability experiment

Direct fluorescence measurements were carried out by transferring an RNase A-infused DNA crystal into 120 µL reaction buffer (4-fold molar excess of RNase inhibitor or MBP-RNase inhibitor, 10 mM NaCaco pH 7.0, 120 mM $Mg(HCO_2)_2$, and 50 mM LiCl) in a cuvette. Fluorescence intensity was monitored (λ_{excit} = 475 nm; λ_{emis} = 522 nm) immediately after RNA substrate was added into the reaction buffer

to a final concentration of 0.63 μM. Indirect fluorescence measurements were carried out by transferring an RNase A-infused DNA crystal into 400 μL reaction solution (0.63 μM RNA substrate, 4-folds excess of MBP-RNase inhibitor, 10 mM NaCaco pH 7.0, 120 mM $Mg(HCO_2)_2$, and 50 mM LiCl). 60 μL (enzymatic kinetics measurement) or 120 μL (reusability test) reaction buffer was taken at different time points. For the reusability experiment, the crystal was washed as described above to remove the RNA substrate and products and then transferred to another reaction solution. Crystals were stored at 4 °C in MFJ buffer for cycles performed on different days.

8.5 Western blot and dot blot analyses

12.5 μL of the 25 μL MFJ buffer containing a dissolved protein-coated RNase A-infused DNA crystal was used for either western blot or dot blot analysis. For western blotting, proteins were separated in 15% SDS-PAGE and transferred to PVDF membrane using Bio-Rad Mini-PROTEAN tank transfer unit. For dot blotting, protein solution was directly added onto nitrocellulose membrane (0.2 μm pore size) and air-dried. Immunodetection was performed using primary antibody against bovine RNase A (ab6610, Abcam, UK) and secondary antibody against rabbit IgG (ab6802, Abcam, UK). The results were visualized by using ECL kit (SuperSignal West Pico Chemiluminescent Substrate, Thermo Fisher Scientific, USA). Densitometry was performed using TotalLab Quant software.

8.6 Confocal microscopy imaging

Confocal fluorescence microscopy was performed on a Leica SP5 X Confocal Microscope at room temperature (λ_{excit} = 488 nm). To initiate the catalytic reaction by RNase A, 1.5 μL of RNA substrate was added into 100 μL of MFJ solution (Final concentration for RNA substrate is 2 μM) containing a protein coated RNase A-infused DNA crystal and 4-folds molar excess of RNase inhibitor.

Chapter 9: Enzyme-infused DNA Crystals as Biocatalyst

9.1 Using RNase A as a model enzyme with dinucleotide RNA substrate/MBP-RNase inhibitor

Bovine pancreatic RNase A was chosen as a model enzyme for this study. RNase A is ~14 kDa,[71] placing it within the range of proteins that can be absorbed into the crystal's channels[61]. It is also highly stable in a variety of reaction conditions and can be assayed using a wide variety of substrates.[72] This study utilized a quenched fluorescent rUA dinucleotide, similar to those used in previous studies[73]. The dinucleotide contained 5' dabcyl and 3' fluorescein moieties to enable fluorescence release upon cleavage of the scissile phosphodiester linkage **(Figure 9.1)**. Importantly, RNase A is also potently inhibited by the protein RNase inhibitor through tight interactions with a femtomolar dissociation constant.[70] With a molecular weight of ~50 kDa, RNase inhibitor is significantly larger than RNase A, placing it slightly above the size limit of proteins that were detected in the crystal interior. However, to avoid RNase inhibitor potentially inhibiting RNase A inside the crystals, an MBP-RNase inhibitor fusion protein (90 kDa; see Chapter 8) was constructed and used interchangeably with commercially available RNase inhibitor.

DNA crystals were loaded with RNase A by soaking 4 days in 44 mg/mL RNase A at 4 °C. Crystals were washed extensively with buffer before being incubated with RNase inhibitor or MBP-RNase inhibitor prior to initiating reactions. Pilot experiments using washed and dissolved crystals established the amount of inhibitor necessary to inhibit all of the RNase present in a medium-sized crystal (defined here as being ~200 μm across the hexagonal base). All activity assays used

4-times this amount of inhibitor to ensure its excess. Immunoblot analysis from several crystals indicated that typical crystals contained ~20 ng of RNase A **(Figure 9.2)**.

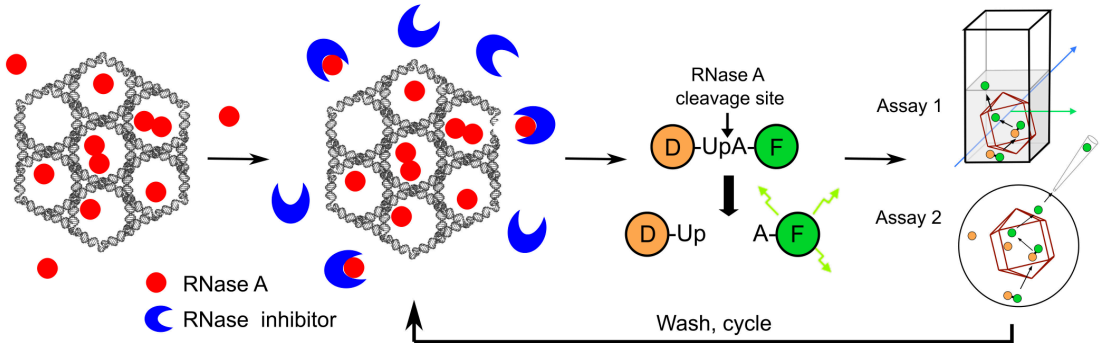

Figure 9.1 - Schematic representation of the fluorescence assays
A single DNA crystal is infused with RNase A and then transferred to buffer containing excessive RNase inhibitor or MBP-RNase inhibitor. The RNase A on the crystal surface or that has diffused out of the crystal will be bound. A dinucleotide RNA substrate containing 5' dabcyl and 3' fluorescein moieties enables fluorescence release upon the cleavage of its scissile phosphodiester linkage by RNase A. Direct fluorescence assay **(Assay 1)** is performed within a low-volume fluorescence cuvette containing reaction buffer and substrate. Fluorescence accumulation was monitored over time without agitation. Indirect assay **(Assay 2)** is performed by having aliquots of the reaction buffer being removed from around the crystals at various time points and the fluorescence measured. Multiple cycles of fluorescence assays are performed following the removal of substrate and products by washing. For both assays excessive RNase inhibitor or MBP-RNase inhibitor is added to the reaction media to ensure the RNase activity monitored is entirely from the crystal-encapsulated RNase A.

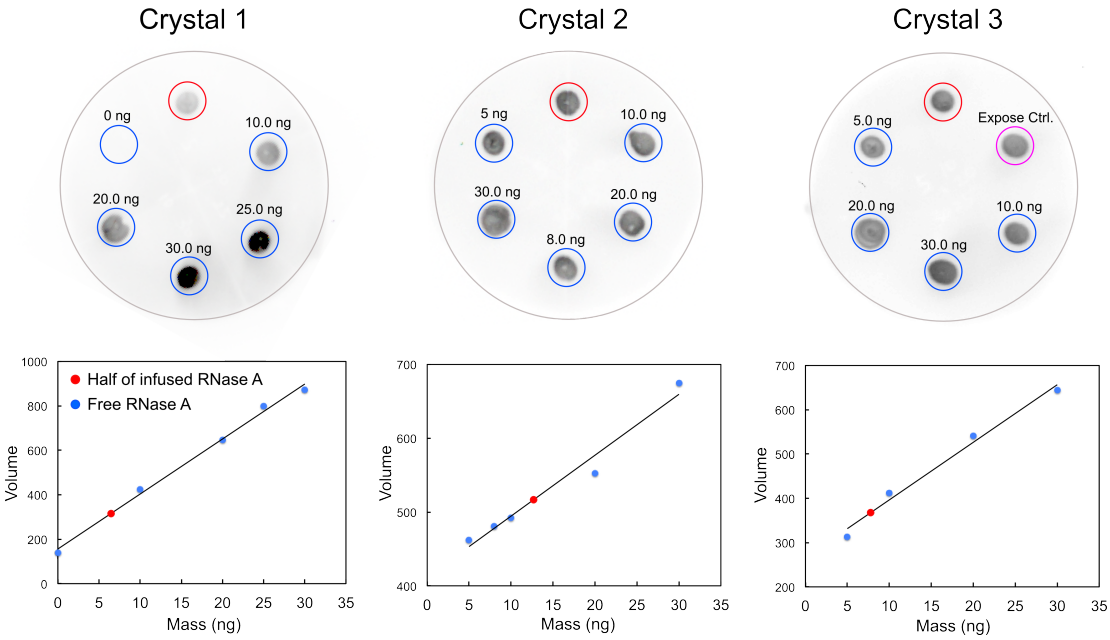

Figure 9.2 - Immunoblot analysis from three RNase A-infused crystals.
Top panel: each crystal was dissolved in 25 µL buffer solution and half of the volume was loaded onto a nitrocellulose membrane together with known aqueous RNase A samples, followed by immunodetection and imaging. The crystal samples are in red circles and the known RNase A samples are in blue circles. Bottom panel: a standard curve of dot volume against the input mass of aqueous RNase A samples was made from the dot blot. The masses of infused RNase A were obtained by fitting the dot volume of the crystal sample into the standard curves and were calculated to be 13.7 ng, 25.2 ng, and 14.6 ng, respectively. These were the three crystals used for kinetic analysis in **Figure 10.4**.

9.2 Direct and indirect fluorometry assays

RNase A activity of loaded crystals was monitored in two ways as described in **Figure 9.1**. Prepared crystals were transferred directly to a low-volume fluorescence cuvette containing reaction buffer and substrate. Fluorescence accumulation was monitored over time without agitation **(Figure 9.3)**. For some crystals anomalous peaks were observed **(Figure 9.4)**, which were attributed primarily to the crystal being in the cuvette light path, but may also be the result of mass transfer effects. Following the initial 3 h reaction, crystals were reused by washing for at least 30 min to remove substrates and products, incubating with fresh inhibitor, and transferring to a new reaction buffer. Similar profiles were observed for multiple cycles, but with decreased overall fluorescence, presumably due to the loss or inactivation of RNase A during the wash steps. Similar results were obtained when the crystals were incubated in the same conditions, but aliquots of the reaction buffer were removed from around the crystals at various time points and the fluorescence measured **(Figure 9.3, inset)**. There was little change in fluorescence intensity of the individual time points over 20 min **(Figure 9.5)**, indicating that any RNase A released into the solution during the assay or washing steps was effectively bound by the inhibitor.

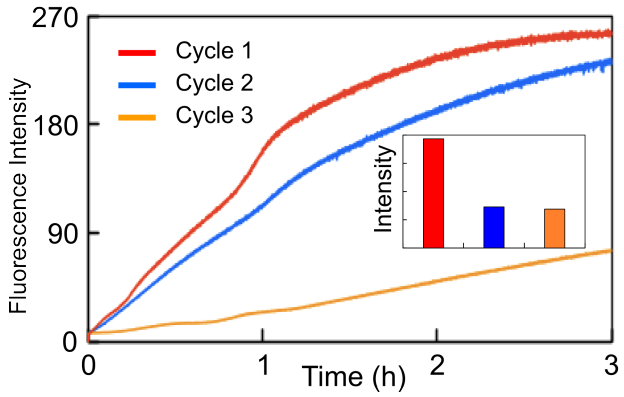

Figure 9.3 - RNase A activity of DNA crystals.
Fluorescence intensities of uncoated single crystal versus time (Direct assay) are shown in the main panel and bulk solution fluorescence (Indirect assay) at a single time point (60') for different crystals are shown in the inset.

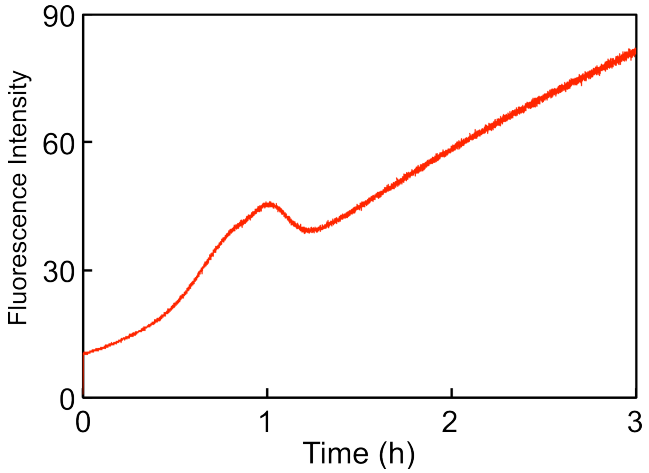

Figure 9.4 - An RNase A-infused crystal shows an anomalous peak with sharp fluorescence changes.
The anomalous peaks at ~1h are primarily attributed to the crystal being in the cuvette light path, but may also be the result of mass transfer effect.

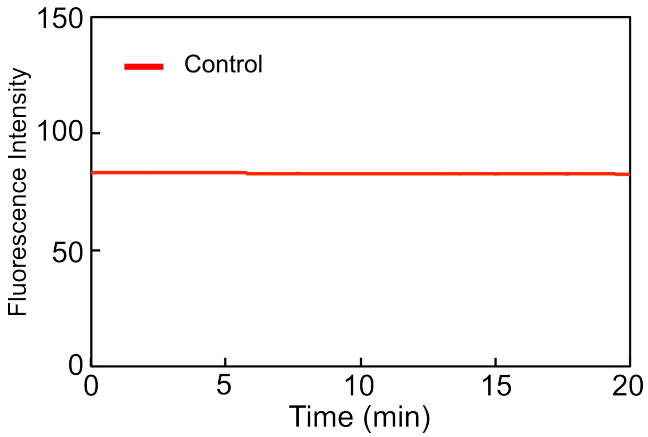

Figure 9.5 - Released RNase A does not contribute to bulk fluorescence.
To check if any RNase A released into the solution during the assay or washing steps is effectively bound by MBP-RNase inhibitor, an aliquot of the reaction buffer taken at 60 minute from the first cycle of a fluorescence assay was monitored for 20 min. The absence of any appreciable gain in signal suggests that any RNase A released is bound by inhibitor. (The reaction sample with RNase inhibitor has the same kinetic profile as MBP-RNase inhibitor)

Chapter 10: Protective Protein-based "Coating" Improves Reusability of an Enzyme-infused DNA Crystal

10.1 Reuse experiment

To improve the reusability of the RNase A infused crystals, a coating technique was developed to prevent the loss of enzyme. Washed crystals were incubated with 30 mg/mL hen egg-white lysozyme solutions for 5 min, and then transferred to fresh buffer containing 2% glutaraldehyde for 20 min. Western blot analysis did not show higher molecular weight RNase A **(Figure 10.1)**, indicating that under these conditions there was little intermolecular crosslinking of the enzyme. Utilizing both assay methods described above, RNase activity profiles for coated crystals were maintained over sequential cycles **(Figure 10.2)**, with up to 4 days between cycles **(Figure 10.3)**.

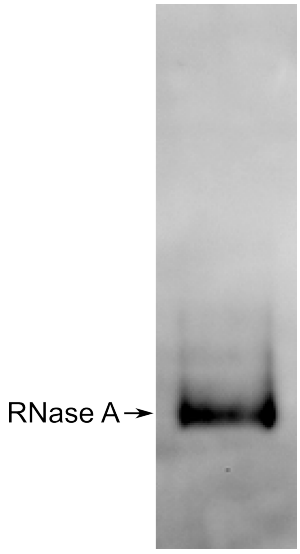

Figure 10.1 - Western blot result of a dissolved RNase-infused crystal.
No significant higher molecular weight RNase A is observed, indicating little or no intermolecular crosslinking of RNase A as a result of glutaraldehyde crosslinking.

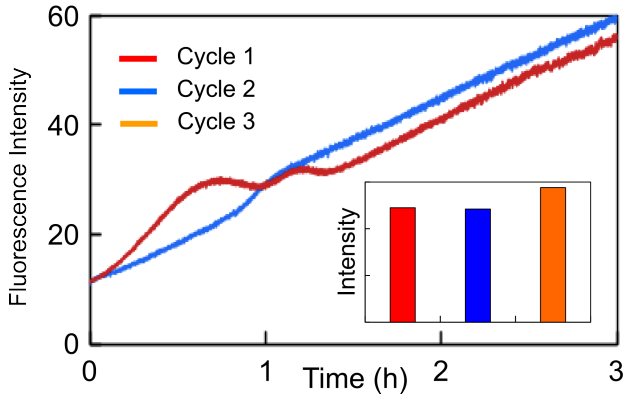

Figure 10.2 - RNase A activity of protein-coated DNA crystals.
Fluorescence intensities of lysozyme-coated single crystal versus time (direct assay) are shown in the main panel and bulk solution fluorescence (Indirect assay) at a single time point (60') for different crystals are shown in the inset. Only 2 cycles are shown for the direct assay.

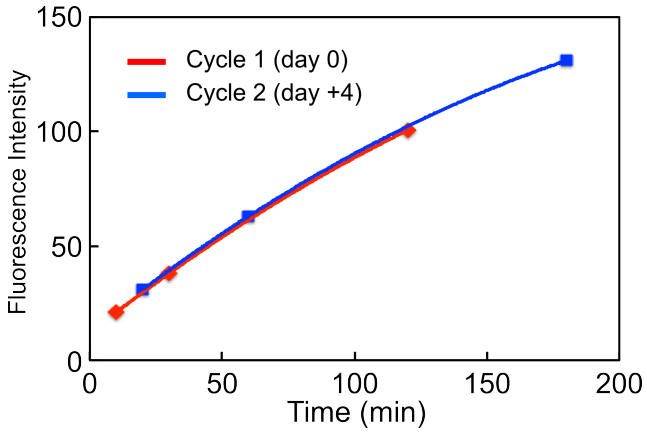

Figure 10.3 - Reusability test of a protein-coated RNase A-infused crystal. Crystal activity profiles are maintained at the same level over multiple sequential cycles. Here, Cycle 2 is performed 4 days after the Cycle 1.

10.2 Steady-state kinetic parameters for encapsulated enzyme

Having crystals that retained activity over multiple cycles allowed me to attempt to determine steady-state kinetic parameters for the encapsulated enzymes. Single lysozyme-coated crystals were incubated at 7 different substrate concentrations sequentially. Aliquots of the reactions were taken at various time points and used to determine initial reaction velocities. Multiple crystals showed good agreement and little difference when the reaction series were done with ascending or descending substrate concentrations. Initial velocities plotted vs. substrate concentrations showed non-hyperbolic saturation kinetics in the measurable substrate range **(Figure 10.4)**. This non-Michaelis-Menten behavior is consistent with other examples of immobilized enzymes[62-67] and can be attributed to the significant mass transfer effects resulting from both external and internal diffusion of substrates and products in such large crystals. These effects can be mitigated at high substrate concentrations,[64] but in this case, testing higher substrate concentrations proved intractable due to the difficulty in obtaining early time points in the linear range. Importantly, because the free enzyme does follow Michaelis-Menten kinetics,[74] this result further supports the conclusion that the observed dinucleotide cleavage events occur inside the crystal.

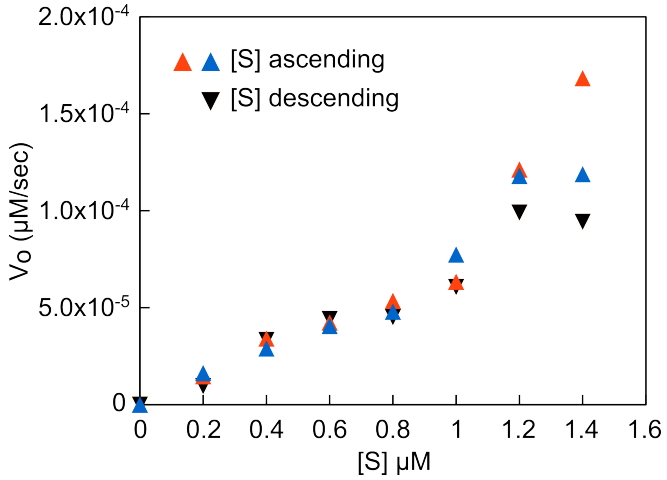

Figure 10.4 - Non-Michaelis-Menten kinetics of RNase A infused crystals. Initial velocities determined from 7 substrate concentrations for three independent crystals were plotted versus substrate concentrations. These show non-hyperbolic substrate dependence. Similar results were obtained with ascending or descending substrate concentrations, with the most variability at the highest substrate.

10.3 Confocal fluorescence microscopy

Confocal microscopy was used to directly visualize the release of fluorescence signal from the crystal **(Figure 10.5)**. Substrate was added to standard reaction conditions containing the crystal and multiple planes were imaged over time. Depending on substrate concentration, detectable localized fluorescence release that was initially most intense around the periphery of the crystal, was observed within 12 min. However, within minutes the interior fluorescence had achieved comparable levels. This is consistent with the encapsulated enzymes closest to the crystal periphery being likely to contact substrate first, while diffusion effects limit substrate accessibility to the more deeply buried enzymes. Interestingly, even at late time points, there was greater fluorescence apparent at six-fold ends of the crystal periphery, possibly indicating preferential product release from the much larger crystal pores present down this axis.

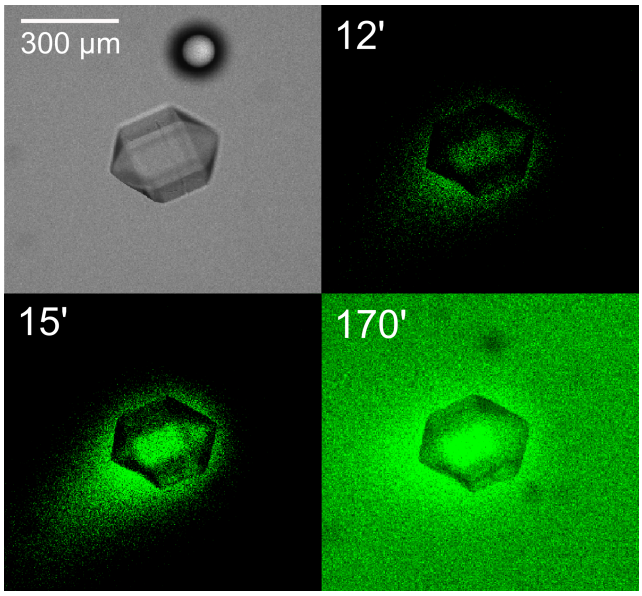

Figure 10.5 - Confocal microscopy of RNA substrate cleavage by a DNA crystal. RNA substrate with a final concentration of 2 µM was added to a single RNase A-infused DNA crystal, which was monitored by confocal microscopy over time.

Chapter 11: Summary and concluding remarks

11.1 Summary of results

Three-dimensional DNA crystals have long been envisioned as containers for biocatalysis. By using RNase A as a model enzyme system I have demonstrated that the crystals infused with enzyme can cleave a dinucleotide substrate with kinetic parameters similar to other reported immobilized enzyme systems[62-67]. The axially distinct aperture sizes in the crystal design allowed me to improve encapsulation of the enzyme with a protective protein-based "coating" cross-linked around the crystal surface. This coating allows entry and exit of small molecules through the crystal while restricting enzymes inside the crystal. The enzyme-infused DNA crystal is capable of performing multiple cycles of catalysis and retaining its enzymatic activity over numerous days after being protein-coated.

11.2 Contributions to present knowledge and future implications

The concepts of the enzyme-infused DNA crystal and the unique protein coating technique provide possibilities to the development of modular solid-state catalysts. The development of solid-state enzymatic catalysts in a DNA framework may have a number of advantages over other crystal-based biocatalysis systems.[64-67] Most significant of these may be the potential to develop modular catalysts by incorporating different enzymes into the crystal solvent channels. A natural extension of these types of modular crystals would be the introduction for multiple enzymes to perform sequential reactions. The observed kinetic restrictions are a problem common to cross-linked protein crystals[66, 67] and the crystals described here. A solution to this

problem with cross-linked protein crystals is to reduce the particle size. This may be achieved with DNA crystals through controlled growth conditions. Though it may be necessary in these cases to crystallize the DNA in the presence of the enzymes to improve incorporation yields. Similar to cross-linked protein crystals,[64-66] these DNA crystals are composed entirely of biomolecules. Although the application of enzyme-infused DNA crystal itself is not a biomedical application, it is biodegradable and potentially biocompatible for environmental or biomedical applications. For example, it can potentially be used in enzyme replacement therapy by protectively delivering specific enzyme to the target organs.

The DNA crystals used in this study have a relatively constant temperature range (> 37°C) over which they become unstable and start to disassemble at a relatively fast rate. And we found by using chemical cross-linkers to stabilize the inter-strand interaction, the disassemble temperature range could be raised and the treated DNA crystals could stay stable for a longer period of time at higher temperatures. This discovery will potentially allow researchers to develop a temperature-controlled release device using such crystals. Similar to the enzyme replacement therapy application using the DNA crystal, a temperature-controlled release crystal can deliver specific drugs to inflammatory tissues where temperature is slightly higher. However, this application needs a more accurate temperature control in both crystal disassemble and drug release, which, at this point, has not been explored yet but will probably be a new direction in the future studies.

References

1. Cech, T. R., and Bass, B. L. (1986) Biological catalysis by RNA, *Annu Rev Biochem 55*, 599-629.
2. Cech, T. R. (1990) Self-splicing of group I introns, *Annu Rev Biochem 59*, 543-568.
3. Adams, P. L., Stahley, M. R., Kosek, A. B., Wang, J., and Strobel, S. A. (2004) Crystal structure of a self-splicing group I intron with both exons, *Nature 430*, 45-50.
4. Guo, F., Gooding, A. R., and Cech, T. R. (2004) Structure of the Tetrahymena ribozyme: base triple sandwich and metal ion at the active site, *Mol Cell 16*, 351-362.
5. Golden, B. L., Kim, H., and Chase, E. (2005) Crystal structure of a phage Twort group I ribozyme-product complex, *Nat Struct Mol Biol 12*, 82-89.
6. Cech, T. R. (1988) Conserved sequences and structures of group I introns: building an active site for RNA catalysis--a review, *Gene 73*, 259-271.
7. Burke, J. M., Belfort, M., Cech, T. R., Davies, R. W., Schweyen, R. J., Shub, D. A., Szostak, J. W., and Tabak, H. F. (1987) Structural conventions for group I introns, *Nucleic Acids Res 15*, 7217-7221.
8. Zaug, A. J., and Cech, T. R. (1987) Self-splicing RNA and an RNA enzyme in Tetrahymena, *J Protozool 34*, 416-417.
9. Lang, B. F., Laforest, M. J., and Burger, G. (2007) Mitochondrial introns: a critical view, *Trends Genet 23*, 119-125.

10. Haugen, P., Simon, D. M., and Bhattacharya, D. (2005) The natural history of group I introns, *Trends Genet 21*, 111-119.

11. Cech, T. R., Zaug, A. J., and Grabowski, P. J. (1981) In vitro splicing of the ribosomal RNA precursor of Tetrahymena: involvement of a guanosine nucleotide in the excision of the intervening sequence., *Cell 27*, 487-496.

12. Zaug, A. J., and Cech, T. R. (1982) The intervening sequence excised from the ribosomal RNA precursor of Tetrahymena contains a 5-terminal guanosine residue not encoded by the DNA, *Nucleic Acids Res 10*, 2823-2838.

13. Michel, F., and Westhof, E. (1990) Modelling of the three-dimensional architecture of group I catalytic introns based on comparative sequence analysis, *J Mol Biol 216*, 585-610.

14. Golden, B. L., Gooding, A. R., Podell, E. R., and Cech, T. R. (1998) A preorganized active site in the crystal structure of the Tetrahymena ribozyme, *Science 282*, 259-264.

15. Paukstelis, P. J., Chen, J. H., Chase, E., Lambowitz, A. M., and Golden, B. L. (2008) Structure of a tyrosyl-tRNA synthetase splicing factor bound to a group I intron RNA, *Nature 451*, 94-97.

16. Costa, M., and Michel, F. (1997) Rules for RNA recognition of GNRA tetraloops deduced by in vitro selection: comparison with in vivo evolution, *EMBO J 16*, 3289-3302.

17. Batey, R. T., Rambo, R. P., and Doudna, J. A. (1999) Tertiary Motifs in RNA Structure and Folding, *Angew Chem Int Ed Engl 38*, 2326-2343.

18. Bokinsky, G., Nivón, L. G., Liu, S., Chai, G., Hong, M., Weeks, K. M., and Zhuang, X. (2006) Two distinct binding modes of a protein cofactor with its target RNA, *J Mol Biol 361*, 771-784.

19. Duncan, C. D., and Weeks, K. M. (2010) The Mrs1 splicing factor binds the bI3 group I intron at each of two tetraloop-receptor motifs, *PLoS One 5*, e8983.

20. Rho, S. B., and Martinis, S. A. (2000) The bI4 group I intron binds directly to both its protein splicing partners, a tRNA synthetase and maturase, to facilitate RNA splicing activity, *RNA 6*, 1882-1894.

21. Bassi, G. S., de Oliveira, D. M., White, M. F., and Weeks, K. M. (2002) Recruitment of intron-encoded and co-opted proteins in splicing of the bI3 group I intron RNA, *Proc Natl Acad Sci U S A 99*, 128-133.

22. Shaw, L. C., and Lewin, A. S. (1995) Protein-induced folding of a group I intron in cytochrome b pre-mRNA, *J Biol Chem 270*, 21552-21562.

23. Caprara, M. G., Chatterjee, P., Solem, A., Brady-Passerini, K. L., and Kaspar, B. J. (2007) An allosteric-feedback mechanism for protein-assisted group I intron splicing, *RNA 13*, 211-222.

24. Akins, R. A., and Lambowitz, A. M. (1987) A protein required for splicing group I introns in Neurospora mitochondria is mitochondrial tyrosyl-tRNA synthetase or a derivative thereof., *Cell 50*, 331-345.

25. Guo, Q., and Lambowitz, A. M. (1992) A tyrosyl-tRNA synthetase binds specifically to the group I intron catalytic core, *Genes Dev 6*, 1357-1372.

26. Mohr, G., Zhang, A., Gianelos, J. A., Belfort, M., and Lambowitz, A. M. (1992) The neurospora CYT-18 protein suppresses defects in the phage T4 td intron by stabilizing the catalytically active structure of the intron core, *Cell 69*, 483-494.

27. Caprara, M. G., Mohr, G., and Lambowitz, A. M. (1996) A tyrosyl-tRNA synthetase protein induces tertiary folding of the group I intron catalytic core, *J Mol Biol 257*, 512-531.

28. Caprara, M. G., Lehnert, V., Lambowitz, A. M., and Westhof, E. (1996) A tyrosyl-tRNA synthetase recognizes a conserved tRNA-like structural motif in the group I intron catalytic core, *Cell 87*, 1135-1145.

29. Myers, C. A., Kuhla, B., Cusack, S., and Lambowitz, A. M. (2002) tRNA-like recognition of group I introns by a tyrosyl-tRNA synthetase, *Proc Natl Acad Sci U S A 99*, 2630-2635.

30. Paukstelis, P. J., and Lambowitz, A. M. (2008) Identification and evolution of fungal mitochondrial tyrosyl-tRNA synthetases with group I intron splicing activity, *Proc Natl Acad Sci U S A 105*, 6010-6015.

31. Saldanha, R. J., Patel, S. S., Surendran, R., Lee, J. C., and Lambowitz, A. M. (1995) Involvement of Neurospora mitochondrial tyrosyl-tRNA synthetase in RNA splicing. A new method for purifying the protein and characterization of physical and enzymatic properties pertinent to splicing, *Biochemistry 34*, 1275-1287.

32. Myers, C. A., Wallweber, G. J., Rennard, R., Kemel, Y., Caprara, M. G., Mohr, G., and Lambowitz, A. M. (1996) A tyrosyl-tRNA synthetase

suppresses structural defects in the two major helical domains of the group I intron catalytic core, *J Mol Biol 262*, 87-104.

33. Chen, X., Mohr, G., and Lambowitz, A. M. (2004) The Neurospora crassa CYT-18 protein C-terminal RNA-binding domain helps stabilize interdomain tertiary interactions in group I introns, *RNA 10*, 634-644.

34. Vicens, Q., Paukstelis, P. J., Westhof, E., Lambowitz, A. M., and Cech, T. R. (2008) Toward predicting self-splicing and protein-facilitated splicing of group I introns, *RNA 14*, 2013-2029.

35. Chadee, A. B., Bhaskaran, H., and Russell, R. (2010) Protein roles in group I intron RNA folding: the tyrosyl-tRNA synthetase CYT-18 stabilizes the native state relative to a long-lived misfolded structure without compromising folding kinetics, *J Mol Biol 395*, 656-670.

36. Jakes, R., and Fersht, A. R. (1975) Tyrosyl-tRNA synthetase from Escherichia coli. Stoichiometry of ligand binding and half-of-the-sites reactivity in aminoacylation, *Biochemistry 14*, 3344-3350.

37. Brick, P., Bhat, T. N., and Blow, D. M. (1989) Structure of tyrosyl-tRNA synthetase refined at 2.3 A resolution. Interaction of the enzyme with the tyrosyl adenylate intermediate, *J Mol Biol 208*, 83-98.

38. Cherniack, A. D., Garriga, G., Kittle, J. D., Akins, R. A., and Lambowitz, A. M. (1990) Function of Neurospora mitochondrial tyrosyl-tRNA synthetase in RNA splicing requires an idiosyncratic domain not found in other synthetases, *Cell 62*, 745-755.

39. Paukstelis, P. J., Coon, R., Madabusi, L., Nowakowski, J., Monzingo, A., Robertus, J., and Lambowitz, A. M. (2005) A tyrosyl-tRNA synthetase adapted to function in group I intron splicing by acquiring a new RNA binding surface, *Mol Cell 17*, 417-428.

40. Mohr, G., Rennard, R., Cherniack, A. D., Stryker, J., and Lambowitz, A. M. (2001) Function of the Neurospora crassa mitochondrial tyrosyl-tRNA synthetase in RNA splicing. Role of the idiosyncratic N-terminal extension and different modes of interaction with different group I introns, *J Mol Biol 307*, 75-92.

41. Studier, F. W. (2005) Protein production by auto-induction in high density shaking cultures, *Protein Expr Purif 41*, 207-234.

42. Ward, W. H., and Fersht, A. R. (1988) Asymmetry of tyrosyl-tRNA synthetase in solution, *Biochemistry 27*, 1041-1049.

43. Hane, J. K., Lowe, R. G., Solomon, P. S., Tan, K. C., Schoch, C. L., Spatafora, J. W., Crous, P. W., Kodira, C., Birren, B. W., Galagan, J. E., Torriani, S. F., McDonald, B. A., and Oliver, R. P. (2007) Dothideomycete plant interactions illuminated by genome sequencing and EST analysis of the wheat pathogen Stagonospora nodorum, *Plant Cell 19*, 3347-3368.

44. Paukstelis, P. J., Chari, N., Lambowitz, A. M., and Hoffman, D. (2011) NMR Structure of the C-terminal domain of a tyrosyl-tRNA synthetase that functions in group I intron splicing, *Biochemistry 50*, 3816-3826.

45. Seeman, N. C. (2003) DNA in a material world, *Nature 421*, 427-431.

46. Ouldridge, T. E., Hoare, R. L., Louis, A. A., Doye, J. P., Bath, J., and Turberfield, A. J. (2013) Optimizing DNA nanotechnology through coarse-grained modeling: a two-footed DNA walker, *ACS Nano 7*, 2479-2490.

47. Gait, M. J., Komiyama, M., Seeman, N. C., Seitz, O., Micklefield, J., and Liu, D. R. (2013) Nucleic acids: new life, new materials, *Org Biomol Chem 11*, 2058-2059.

48. Chandran, H., Rangnekar, A., Shetty, G., Schultes, E. A., Reif, J. H., and LaBean, T. H. (2013) An autonomously self-assembling dendritic DNA nanostructure for target DNA detection, *Biotechnol J 8*, 221-227.

49. Rothemund, P. W. (2006) Folding DNA to create nanoscale shapes and patterns, *Nature 440*, 297-302.

50. Winfree, E., Liu, F., Wenzler, L. A., and Seeman, N. C. (1998) Design and self-assembly of two-dimensional DNA crystals, *Nature 394*, 539-544.

51. Liu, D., Wang, M., Deng, Z., Walulu, R., and Mao, C. (2004) Tensegrity: construction of rigid DNA triangles with flexible four-arm DNA junctions, *J Am Chem Soc 126*, 2324-2325.

52. Shih, W. M., Quispe, J. D., and Joyce, G. F. (2004) A 1.7-kilobase single-stranded DNA that folds into a nanoscale octahedron, *Nature 427*, 618-621.

53. Andersen, E. S., Dong, M., Nielsen, M. M., Jahn, K., Subramani, R., Mamdouh, W., Golas, M. M., Sander, B., Stark, H., Oliveira, C. L., Pedersen, J. S., Birkedal, V., Besenbacher, F., Gothelf, K. V., and Kjems, J. (2009) Self-assembly of a nanoscale DNA box with a controllable lid, *Nature 459*, 73-76.

54. Majumder, U., Rangnekar, A., Gothelf, K. V., Reif, J. H., and LaBean, T. H. (2011) Design and construction of double-decker tile as a route to three-dimensional periodic assembly of DNA, *J Am Chem Soc 133*, 3843-3845.

55. Seeman, N. C. (1982) Nucleic acid junctions and lattices, *J Theor Biol 99*, 237-247.

56. Sha, R., Birktoft, J. J., Nguyen, N., Chandrasekaran, A. R., Zheng, J., Zhao, X., Mao, C., and Seeman, N. C. (2013) Self-assembled DNA crystals: the impact on resolution of 5'-phosphates and the DNA source, *Nano Lett 13*, 793-797.

57. Zheng, J., Birktoft, J. J., Chen, Y., Wang, T., Sha, R., Constantinou, P. E., Ginell, S. L., Mao, C., and Seeman, N. C. (2009) From molecular to macroscopic via the rational design of a self-assembled 3D DNA crystal, *Nature 461*, 74-77.

58. Robinson, B. H., and Seeman, N. C. (1987) The design of a biochip: a self-assembling molecular-scale memory device, *Protein Eng 1*, 295-300.

59. Ribeiro, F. R., Alvarez, F., Henriques, C., Lemos, F., Lopes, J.M., Ribeiro, M.F. (**1995**) Structure-activity relationship in zeolites, pp 245–270, *J. Mol. Catal. A., Chem.*

60. Paukstelis, P. J., Nowakowski, J., Birktoft, J. J., and Seeman, N. C. (2004) Crystal structure of a continuous three-dimensional DNA lattice, *Chem Biol 11*, 1119-1126.

61. Paukstelis, P. J. (2006) Three-dimensional DNA crystals as molecular sieves, *J Am Chem Soc 128*, 6794-6795.

62. Pedruzzi, I., da Silva, E. A., and Rodrigues, A. E. (2011) Production of lactobionic acid and sorbitol from lactose/fructose substrate using GFOR/GL enzymes from Zymomonas mobilis cells: a kinetic study, *Enzyme Microb Technol 49*, 183-191.

63. Valencia, P., Flores, S., Wilson, L., and Illanes, A. (2011) Effect of internal diffusional restrictions on the hydrolysis of penicillin G: reactor performance and specific productivity of 6-APA with immobilized penicillin acylase, *Appl Biochem Biotechnol 165*, 426-441.

64. Tischer, W., and Kasche, V. (1999) Immobilized enzymes: crystals or carriers?, *Trends Biotechnol 17*, 326-335.

65. Spiess, A., Schlothauer, R., Hinrichs, J., Scheidat, B., and Kasche, V. (1999) pH gradients in immobilized amidases and their influence on rates and yields of beta-lactam hydrolysis, *Biotechnol Bioeng 62*, 267-277.

66. Margolin, A. L., and Navia, M. A. (2001) Protein Crystals as Novel Catalytic Materials, *Angew Chem Int Ed Engl 40*, 2204-2222.

67. St Clair, N. L., and Navia, M. A. (1992) Cross-linked enzyme crystals as robust biocatalysts, *J Am Chem Soc 114,* 7314–7316.

68. Katchalski-Katzir, E. (1993) Immobilized enzymes--learning from past successes and failures, *Trends Biotechnol 11*, 471-478.

69. Tischer, W., and Wedekind, F. (**1999**) *Topics in Current Chemistry: Immobilized Enzymes: Methods and Applications*, Vol. *200*, *Springer Verlag Berlin Heidelberg*.

70. Klink, T. A., Vicentini, A. M., Hofsteenge, J., and Raines, R. T. (2001) High-level soluble production and characterization of porcine ribonuclease inhibitor, *Protein Expr Purif 22*, 174-179.

71. Raines, R. T. (1998) Ribonuclease A, *Chem Rev 98*, 1045-1066.

72. Kelemen, B. R., Klink, T. A., Behlke, M. A., Eubanks, S. R., Leland, P. A., and Raines, R. T. (1999) Hypersensitive substrate for ribonucleases, *Nucleic Acids Res 27*, 3696-3701.

73. Park, C., Kelemen, B. R., Klink, T. A., Sweeney, R. Y., Behlke, M. A., Eubanks, S. R., and Raines, R. T. (2001) Fast, facile, hypersensitive assays for ribonucleolytic activity, *Methods Enzymol 341*, 81-94.

74. Park, C., and Raines, R. T. (2003) Catalysis by ribonuclease A is limited by the rate of substrate association, *Biochemistry 42*, 3509-3518.